

DelDOT Final Report

submitted to DelDOT

**NON-DESTRUCTIVE TESTING METHODS TO  
EVALUATE THE INTEGRITY OF CONCRETE BRIDGE  
DECKS**

Task Number 57-1490

Thomas Schumacher, Associate Professor, PhD, PE (DE)

December 22, 2021  
Portland State University

## TABLE OF CONTENTS

<b>1</b>	<b>INTRODUCTION AND OVERVIEW</b> .....	<b>1</b>
<b>2</b>	<b>GROUND PENETRATING RADAR</b> .....	<b>2</b>
2.1	Introduction .....	2
2.1.1	Background.....	2
2.1.2	Basics of GPR Testing.....	3
2.1.3	Motivation .....	4
2.2	Setup and Methods .....	4
2.2.1	Description of GPR Device .....	4
2.2.2	Transmitted Pulse and Time-Zero Off-Set.....	5
2.2.3	Proposed Data Analysis Procedure .....	6
2.3	Laboratory Tests.....	8
2.3.1	Concrete Blocks.....	8
2.3.2	Laboratory Bridge Mock-up Specimens .....	10
2.4	Summary and Conclusions .....	18
2.5	Acknowledgements .....	19
2.6	Field Application Example.....	19
<b>3</b>	<b>IMPULSE RESPONSE TESTING</b> .....	<b>21</b>
3.1	Background and Motivation.....	21
3.2	Test Methodology.....	24
3.3	Numerical Study .....	27
3.3.1	Modeling.....	27
3.3.2	Results and Discussion .....	28
3.4	Experimental Study .....	30
3.4.1	Description of Structure Used for Evaluation .....	30
3.4.2	Test Setup and Procedure .....	31
3.4.3	Sources of Nonlinearity .....	33
3.5	Results and Discussion .....	34
3.5.1	Verification of Results from Individual Test Points.....	34
3.5.2	Comparison of Results with Removed Concrete.....	37
3.6	Summary and Conclusions .....	40
3.7	Acknowledgements .....	41
<b>4</b>	<b>SUMMARY AND CONCLUSIONS</b> .....	<b>42</b>
<b>5</b>	<b>REFERENCES</b> .....	<b>44</b>

## LIST OF TABLES

Table 1. Six selected test point coordinates and their NVI; “very soft” = reference case. ....	35
--	----

## LIST OF FIGURES

Fig. 1. Photo of a severely deteriorated reinforced concrete bridge deck. ....	vii
Fig. 2. Scanning of a concrete bridge deck using hand-held ground penetrating radar (GPR) instrument.....	viii
Fig. 3. Impulse response (IR) testing of a concrete bridge deck. ....	ix
Fig. 4. Hand-held GPR device used in study: (a) photo, (b) elevation view with pertinent dimensions and parameters. T = transmitting antenna, R = receiving antenna. Unit conversion: 216 mm = 8.5 in. ....	5
Fig. 5. Examples of (a) normalized transmitted pulse and (b) received sample signals. The reflected pulse amplitude, $A_{GPR}$ corresponds to the first peak in the waveform. Comment: The transmitted signal was created based on observed received signals. ....	6
Fig. 6. Overview of proposed data processing steps illustrated on an A-scan. ....	7
Fig. 7. Illustration of test setup for basic tests on unreinforced concrete block. ....	9
Fig. 8. Selected A-scans collected from concrete test block: (a) Different back wall materials, (b) concrete on steel with variable air gap, and (c) concrete on concrete with variable air gap. The vertical dotted line at $d = 154$ mm (6.06 in) represents the thickness of the concrete test block. Relative dielectric constant, $\epsilon_r = 6.4$ . Unit conversion example: 12.7 mm = 0.5 in. ....	10
Fig. 9. Drawings of laboratory mock-up specimens: (a) and (b) lightly reinforced (top layer) specimens with variable thickness, (c) bridge deck specimen with artificial delaminations and stay-in-place formwork section, and (d) bridge girder specimen with variable rebar dimensions and concrete cover and two empty post-tensioning ducts. All dimensions are in (mm). Unit conversion example: 305 mm = 12 in.....	12
Fig. 10. (a) Reflected pulse amplitude from rebar, (b) B-scan, and (c) cross-correlation results for Specimen 1a. Relative dielectric constant, $\epsilon_r = 8.0$ . Unit conversion example: 305 mm = 12 in. ....	13
Fig. 11. (a) Reflected pulse amplitude from rebar, (b) B-scan, and (c) cross-correlation results for Specimen 1b. Relative dielectric constant, $\epsilon_r = 8.0$ . Unit conversion example: 305 mm = 12 in. ....	14

Fig. 12. (a) Reflected pulse amplitudes from rebars, (b) B-scan, and (c) cross-correlation results for Specimen 2, Side 1. Relative dielectric constant, $\epsilon_r = 9.0$ . Unit conversion example: 305 mm = 12 in. ....	15
Fig. 13. (a) Reflected pulse amplitudes from rebars, (b) B-scan, and (c) cross-correlation results for Specimen 3, Side 1. Relative dielectric constant, $\epsilon_r = 10.5$ . Unit conversion example: 305 mm = 12 in. ....	16
Fig. 14. (a) Reflected pulse amplitudes from rebars, (b) B-scan, and (c) cross-correlation results for Specimen 3, Side 2. Relative dielectric constant, $\epsilon_r = 10.5$ . Unit conversion example: 305 mm = 12 in. ....	16
Fig. 15. Correlation of actual vs. observed depth for all laboratory mock-up specimens. The dashed-dotted and dotted lines represent mean and 95% prediction limits, respectively. Unit conversion example: 250 mm = 9.84 in.....	17
Fig. 16. Reflected pulse amplitudes from rebar vs. depth for (a) all three lab specimens and (b) for #6 rebars in Specimen 3. Unit conversion example: 70 mm = 2.76 in. ....	18
Fig. 17. GPR results for Deck #3: (a) Plan view of deck and (b) B-scans. Yellow arrows mark lines on the scans that had been determined as delaminated by hammer sounding. Red + mark the locations for which IR measurements were performed, which are discussed in Chapter 3. Unit conversion: 4 ft = 1.22 m. ...	20
Fig. 18. Illustration of test setup used in this study. ....	25
Fig. 19. Sample FRFs for test point A1 [see Fig. 24 (a)] on the selected bridge deck.	26
Fig. 20. Sample $R^2$ -frequency relationship for two FRFs [very soft and very strong from test point A1, see Fig. 26 (a)] vs. frequency and corresponding NVI. ....	27
Fig. 21. Illustration of the 2D finite element (FE) model for Model 2. The red line indicates the delamination (gap). The red point at the surface indicates the acceleration measurement point. The purple arrows indicate the distributed force applied on the deck. ....	28
Fig. 22. Two sample FRFs for deck models with and without delamination; amplitude of impact force = 4 kN (0.9 kip). ....	29
Fig. 23. Three sample FRF peaks (first peak) for impact forces with amplitudes, 0.5, 4 and 15 kN (0.112, 0.9, and 3.37 kip): (a) Model 1 (without delamination, reference) and (b) Model 2 (with delamination). ....	29
Fig. 24. FRF peak ratio vs. peak impact force value for the two FE models. ....	30

Fig. 25. Branchport Avenue Bridge in Long Branch, NJ: (a) Google map image showing plan view and selected deck (#2) used as part of this study, (b) photo of Deck #2 from a driver’s perspective, and (c) bridge cross-section with dimensions in (in = “) and (ft = ‘). Unit conversion: 1 in = 25.4 mm, 1 ft = 0.305 m. .... 31

Fig. 26. (a) Plan view photo of Deck #2 with test grid (red ‘+’),  $\Delta = 0.61$  m (2 ft), locations of sample test points A1, A2, B1, B2, C1, and C2, and extracted concrete cores (full black circles). (b) Peak impact forces for all 270 test points. Unit conversion: 20 kN = 4.5 kip. .... 32

Fig. 27. Samples of (a) four impact forces and (b) corresponding acceleration responses for one select test point. Unit conversion: 15.6 kN = 3.5 kip. .... 33

Fig. 28. Theoretical Stress-Strain relationship and actual generated stress ranges due to “very soft” (grey area) and “very strong” (green area) impact forces (ranges span mean +/- two standard deviations). The black dashed horizontal line represents the suggested linear limit (*LL*). .... 33

Fig. 29.  $R^2$ - frequency relationships for test point A2 (a), B1 (b), B2 (c), C1 (d), and C2 (e). Locations of these test points are shown in Fig. 26 (a). Photos of extracted cores corresponding to (a) and (b) are shown in Fig. 30. Note that the  $R^2$ - frequency relationships for test point A1 is shown in Fig. 20. .... 36

Fig. 30. Photos of extracted concrete cores: (a) Core 1 (near A2) and (b) Core 2 (near B1). .... 36

Fig. 31. Contour plots for (a) NVI values and (b) depth of removed concrete for Deck #2. Circles depict select test points discussed in more detail in Section 3.5.1. Unit conversion: 1 ft = 0.305 m. .... 38

Fig. 32. NVI - Depth of removed concrete vs. NVI correlation plot. Orange and blue dots correspond to data points from within the grey and black dashed boxes, respectively, shown in Fig. 31. The red dash-dotted line and blue dotted lines represent the mean prediction curve and 95% prediction limits, respectively. Unit conversion: 1 ft = 0.305 m. .... 39

## EXECUTIVE SUMMARY

Nationwide, a significant percentage of concrete bridge decks of reinforced and prestressed concrete bridges are exposed not only to a growing traffic volume but also to an increasingly aggressive environment. These conditions can lead to degradation in form of delaminations within the deck. Once large portions of a deck are delaminated, the function of the deck as integral part of the structure may become compromised. An example of a reinforced concrete bridge deck that exhibited severe degradation, and that was evaluated as part of this research, is provided in Fig. 1. Note that the bridge deck was rehabilitated in 2013. So far, transportation agencies have used simple visual inspection and sounding methods, which are often subjective and qualitative, to locate deteriorated areas for repair. These methods give only a rough estimate of the location of the actual deterioration and provide no information about the depth of a delamination. In this research the effectiveness of two non-destructive testing (NDT) methods and their ability to detect and estimate the extent and depth of shallow delaminations in concrete bridge decks were evaluated.



**Fig. 1.** Photo of a severely deteriorated reinforced concrete bridge deck.

Two inexpensive and easy-to-deploy NDT methods, i.e., ground penetrating radar (GPR) and impulse response (IR) testing, were reviewed and evaluated in the laboratory

as well as the field. Modifications related to data analysis of these two methods are proposed, specifically to detect and quantify shallow delaminations.

GPR has the ability to provide valuable information with respect to geometry and location of reinforcing bars, and, in some cases, areas of deterioration such as corrosion or potential delaminations. In this research, a consistent methodology to process and interpret data from a hand-held GPR instrument was developed first. These small devices are often used by practitioners to more accurately inspect areas of interest while traffic control is maintained. An example of an ongoing GPR scan is provided in Fig. 2. The proposed methodology uses an accurate non-linear time-depth relationship and cross-correlation to locate and visualize reflectors. The polarity and amplitude of the reflected pulse is also extracted and gives further information about the type of reflector, e.g., air vs. steel. Data collected and processed from three laboratory mock-up specimens are presented and discussed, and further research is proposed. Finally, data from an in-service bridge deck is discussed.



**Fig. 2.** Scanning of a concrete bridge deck using hand-held ground penetrating radar (GPR) instrument.

IR testing has been performed for many decades to evaluate deep foundations as well as concrete plates. An example of an ongoing IR test on a concrete bridge deck is provided in Fig. 3. As part of this research, a self-referencing NDT method that builds

on IR testing to detect damage using nonlinear vibration characteristics was developed. The hypothesis was that for an undamaged deck, varying the impact force applied to a specific test point does not affect the corresponding frequency response function (FRF) for frequencies that lie within the measurement system's linear operating range. On the other hand, the FRFs for a test point that contains damage changes when the impact force is increased, indicating a nonlinear vibration response. To demonstrate that the concept works theoretically, two 2D finite element (FE) models of a bridge deck, one containing a shallow delamination, were developed and their responses to impact forces of increasing amplitude compared. IR data from an in-service bridge deck was processed and analyzed. Visual inspection results and ultra-high-pressure hydro-blasting performed on the deck as part of a rehabilitation in 2013 provided an opportunity to compare the obtained results with common inspection methods and actual damage extent. Based on the observations, a new damage index, referred to as nonlinear vibration index (NVI), is proposed and shown to be sensitive to damage, including shallow delaminations that were missed by means of hammer sounding.



**Fig. 3.** Impulse response (IR) testing of a concrete bridge deck.

# 1 INTRODUCTION AND OVERVIEW

This document has five chapters, of which the content of Chapters 2 and 3 are published as peer-reviewed journal articles in *Construction and Building Materials*, i.e., Clem et al. (2015) and Hafiz et al. (2022), respectively. One M.S. Thesis (Clem 2013) and one conference paper (Clem et al. 2013) further resulted from this research.

The use of an inexpensive easy-to-deploy hand-held ground penetrating radar (GPR) instrument to evaluate concrete bridge decks is discussed in Chapter 2. While not as reliable as impulse response (IR) testing to discern delaminations, it provides a useful 2D image of the interior revealing rebars and potential areas of degradation. The method is evaluated on laboratory mock-up specimens that contain features of interest as well as an in-service concrete bridge deck.

Chapter 3 describes the development of a modified analysis for impulse response (IR) testing data for the detection of damage in concrete bridge decks. Bases on the work and findings described in Clem (2013) and Clem et al. (2013 and 2015), conventional IR data analysis might not be sensitive enough to detect delaminations, especially during their early stages. The proposed modified analysis uses a so-called nonlinear vibration index (NVI), which is based on non-linear vibration characteristics (Hafiz et al. 2022). It utilizes the same equipment as conventional IR testing but promises higher sensitivity to detect the onset of delaminations as well as distributed damage. The proposed NVI method is evaluated via a 2D finite element (FE) model and measurements taken on an in-service concrete bridge deck.

Chapter 4 summarizes the performed work and provides suggestions for future research and Chapter 5 contains the references of all chapters.

The work discussed in this report has been carried out over the course of one decade. Major support was provided through a research project sponsored by the Delaware Department of Transportation (DelDOT), Task Number 57-1490. Additional funding and other forms of support are acknowledged in Sections 2.5 and 3.7.

## 2 GROUND PENETRATING RADAR

The content of Sections 2.1 through 2.5 is based on the following journal article:

Clem, D. J., Schumacher, T., and Deshon, J. P. (2015). A Consistent Approach for Processing and Interpretation of Data from Concrete Bridge Members Collected with a Hand-Held GPR Device. *Construction and Building Materials*. Vol. 86, pp. 140-148. DOI: <https://doi.org/10.1016/j.conbuildmat.2015.03.105>.

### 2.1 Introduction

#### 2.1.1 Background

Ground penetrating radar (GPR) has been used for many years for subsurface investigations of concrete structures (Bungey 2004). Recently, increased interest in the industry has been focused on the investigation of concrete bridge decks, e.g. (Gucunski et al. 2011; Beben et al. 2012; Xie et al. 2012; Alani et al. 2013). Somewhat commonly, air-coupled (horn) antennas mounted to vehicles are used for scanning of bridge decks occasionally at posted speeds, e.g. (Maser 1996; Barnes and Trottier 2000; Romero et al. 2000; ASTM 2008), with accuracy generally sufficient for network-level comparisons: determining relative deterioration quantities among several decks for planning/budgeting purposes and prioritizing multi-year maintenance activity. Yet, most practitioners employ the use of ground-coupled antennas, with higher-resolution scanning that is achievable only with traffic control, particularly when project-level accuracy in precisely locating affected areas and determining removal quantities are paramount, e.g. (Gucunski et al. 2009; Gucunski et al. 2011).

The analyses for either type of data is different, and is more exacting with the higher-resolution, ground-coupled GPR data. The proposed data processing steps vary from simple visual interpretation of B-scans to complex tomography-based approaches (Valle et al. 1999). The use of GPR scanning for concrete bridge decks can have several goals such as [ordered from greatest to lowest reliability of detection, acc. to Bungey (2004)]:

- Location of reinforcing bars, prestressing strands, metallic ducts, and estimation of their depth, e.g. (Shah et al. 2005; Soldovieri et al. 2006; Dos Santos et al. 2014)
- Estimation of element thickness, e. g. deck underside: possible if no strong reflectors, e.g. (Stryk 2013)
- Locations of corroded reinforcing bars, e.g. (Hong et al. 2012; Alani et al. 2013)
- Locations of moisture variations, e.g. (Binda et al. 1994; Hugenschmidt and Loser 2007; Louis, Van Der Wielen et al. 2012)

- Location and dimensions of air voids, e.g. (Cassidy et al. 2011; Xie et al. 2012; Xie et al. 2013)
- Location of honeycombing or cracking, e.g. (Benedetto 2013)
- Estimation of reinforcing bar sizes, e.g. (Chang et al. 2009; Muniappan et al. 2012)

In this research, alternatively, the use of a comparatively inexpensive hand-held GPR device [see Figs. 2 and 4 (a)] to scan bridge decks with no asphalt overlay is investigated (Clem 2013). To process and interpret the data, a consistent approach using an exact time-depth relationship was implemented. Finally, a procedure based on cross-correlation is proposed for easier interpretation of the raw B-scan data.

### 2.1.2 Basics of GPR Testing

The principal behind GPR testing is relatively simple: A short electromagnetic pulse is transmitted from an internal antenna into the material of interest. This pulse travels from the antenna through the material at a speed inversely proportional to the material's relative dielectric constant, as shown in Eq. 1. This pulse has a center frequency typically ranging anywhere from 400 MHz to 2.6 GHz or higher for concrete applications (ACI 2013). Lower frequency pulses can penetrate deeper into the concrete but have lower resolution compared to higher frequency pulses. Typically, antenna center frequencies below 1 GHz are rarely used except when reinforcement is located relatively deep within the structure, such as thick slab decks, or arched-backfilled bridges with a complete pavement system built on top of the concrete structure. Attenuation of the GPR signal is mainly governed by the electric conductivity which is influenced by moisture content and presence of chlorides (Bungey 2004; Tarussov et al. 2013). A description of the hand-held GPR device used for this research is presented in detail in Section 2.2.1.

The speed of an electromagnetic wave in a material is given by the following equation:

$$c_{material} = \frac{c_{air}}{\sqrt{\epsilon_r}} \quad (1)$$

where  $c_{air}$  is the speed in air (vacuum), equal to 300 mm/ns (11.8 in/ns),  $c_{material}$  is the speed in a specific material, and  $\epsilon_r$  is the relative dielectric constant. Typical values for  $\epsilon_r$  for concrete vary between 6 and 11, for water at 20 °C (68 °F) it is 80, and for steel a practical value of 10,000 is usually used. Per definition, air (vacuum) has a value of 1. Using Eq. 1,

the speed in concrete can be calculated and found to vary between 90 and 120 mm/ns (3.54 and 4.72 in/ns) and for steel it is ca. 34 mm/ns (1.34 in/ns).

The fundamental principle of GPR testing is based on the idea that electromagnetic waves are reflected when they arrive at a material layer with a different dielectric constant (ACI 2013). It is these reflections that are then analyzed. Using Eq. 2, the reflection coefficient,  $\rho$  can be calculated as follows:

$$\rho = \frac{A_{reflected}}{A_{incident}} = \frac{\sqrt{\epsilon_{r,2}} - \sqrt{\epsilon_{r,1}}}{\sqrt{\epsilon_{r,1}} + \sqrt{\epsilon_{r,2}}} \quad (2)$$

where indices 1 and 2 correspond to the material layer the wave is traveling in and the material layer it is arriving at, respectively. The reflection coefficient,  $\rho$  also represents the ratio of reflected vs. incident pulse amplitude. For example, if an electromagnetic pulse with an amplitude of 1 is traveling in a concrete specimen and arrives the back wall of the specimen represented by air, the reflected pulse at the boundary can be expected to have an amplitude of -0.55 to -0.42, corresponding to the reflection coefficient,  $\rho$ . In this case, the pulse is reflected at the boundary and changes polarity. The remaining energy is transmitted past the back wall into the air. Analogous, for the interaction between concrete–water and concrete–steel, the reflection coefficients are  $\rho = 0.5$  and  $\rho = 1.00$ , respectively. Thus, steel represents a perfect reflector that prevents any energy from passing by, effectively shading the areas behind the reflector. Obviously, the actual signal pulse amplitudes measured when they arrive back at the GPR device are smaller due to signal attenuation in the material.

### 2.1.3 Motivation

The objective of this study was to evaluate the use of a comparatively inexpensive hand-held GPR device, combined with simple but accurate and consistent data processing steps, to inspect reinforced concrete bridge decks.

## 2.2 Setup and Methods

### 2.2.1 Description of GPR Device

The hand-held GPR device used for this study is a JRC NJJ-105 Handy Search and is shown in Fig. 4 (a). The device is equipped with two bow-tie dipole antennas denoted T and R, denoting transmitting and receiving antenna, respectively [Fig. 4 (b)]. Also shown in Fig.

4 (b) is an idealized vertical path (dashed line) and actual (full line) raypath. The horizontal off-set of the two antennas,  $d_x = 38$  mm and the stand-off distance,  $d_0 = 4.1$  mm (0.161 in), though this configuration is regarded as ground-coupled, nonetheless. The GPR device records a signal (or A-scan) every 2.5 mm (0.1 in) for a duration of 8 ns at a sampling rate of 64 GHz. Due to the physical length of the device, no data is recorded at the beginning and end of a scan over a distance of  $216$  mm/2 =  $108$  mm ( $8.5$  in/2 =  $4.25$  in).

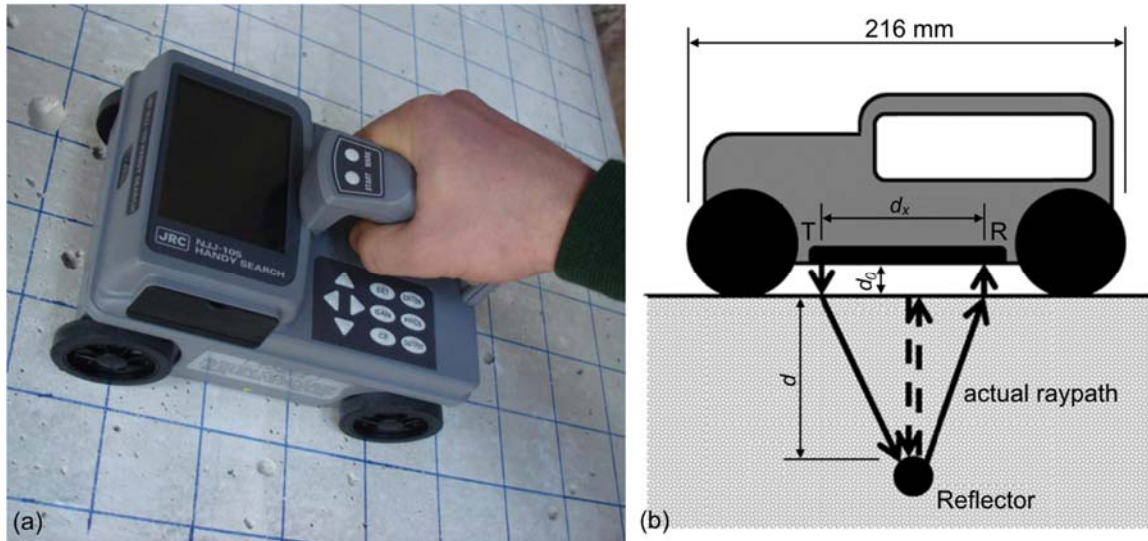


**Fig. 4.** Hand-held GPR device used in study: (a) photo, (b) elevation view with pertinent dimensions and parameters. T = transmitting antenna, R = receiving antenna. Unit conversion:  $216$  mm =  $8.5$  in.

### 2.2.2 Transmitted Pulse and Time-Zero Off-Set

The details of the GPR device needed to be determined to allow for consistent modeling of the wave travel path and quantitative analysis of recorded data. One of the challenges is that the transmitted pulse is not directly known or observable. Also, a time-zero off-set,  $t_0$  exists, which is also unknown. Fig. 5 illustrates the time-zero off-set,  $t_0$  discussed in (Viriyametanont et al. 2008) which exists due to the fact that the recording of signals does not start until the direct wave (aka. breakthrough signal) traveling along the air gap between specimen surface and the GPR device reaches the receiving antenna (R). The time-zero off-set can be simply calculated as follows:

$$t_0 = \frac{d_x}{c_{air}} = \frac{38 \text{ mm}}{300 \text{ mm/ns}} \approx 0.13 \text{ ns} \quad (3)$$

Fig. 5 (a) shows the normalized transmitted pulse and Fig. 5 (b) a sample of a recorded signal from a steel reflector, which has a peak frequency of approximately 1.6 GHz. The direct wave, which travels along the small air gap, was removed by subtracting a reference A-scan taken without any reflectors. The location of interest on the received signal is labeled in Fig. 5 (b). The total pulse travel time,  $t$  corresponds to the actual raypath shown in Fig. 4 (b).

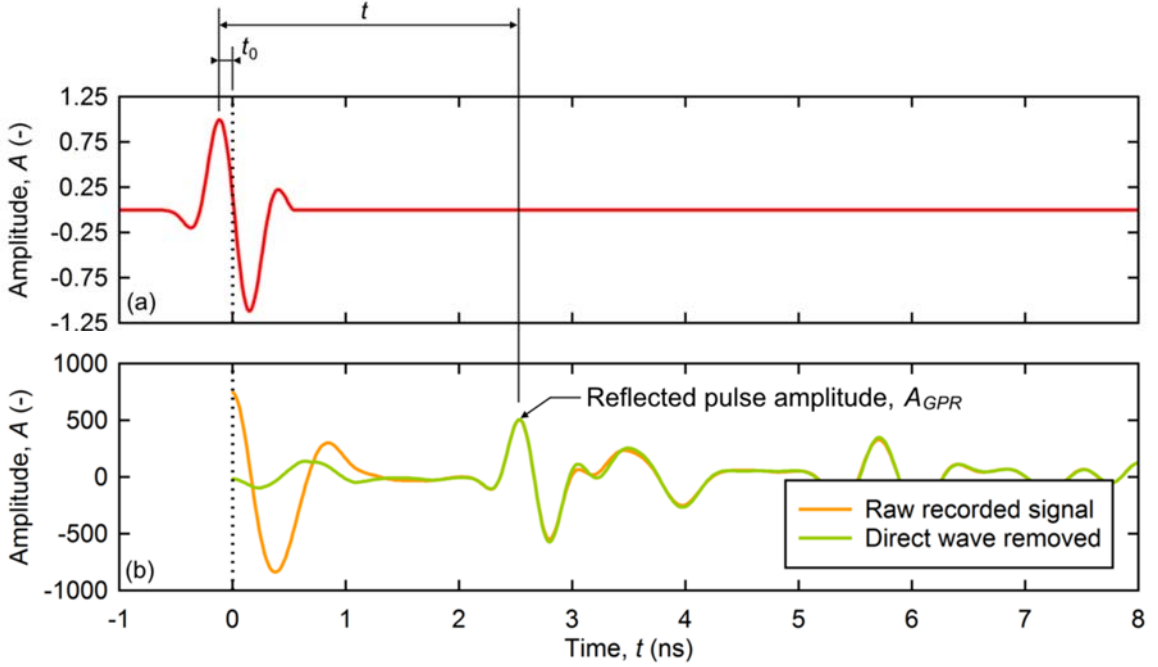


**Fig. 5.** Examples of (a) normalized transmitted pulse and (b) received sample signals. The reflected pulse amplitude,  $A_{GPR}$  corresponds to the first peak in the waveform. Comment: The transmitted signal was created based on observed received signals.

### 2.2.3 Proposed Data Analysis Procedure

An important step to consider is the fact that the transmitting antenna (T) and the receiving antenna (R) are off-set by a horizontal distance,  $d_x = 38$  mm (1.5 in) and a simple linear time-depth relationship as is typically used to calculate depth,  $d$  from signal time,  $t$  will produce significant errors up to 40% for shallow reflectors (Clem 2013). In this research, the actual time-depth relationship based on the actual raypath was employed, as illustrated in Fig. 4 (b). The proposed formulation used for this study is as follows:

$$d(t) = \sqrt{\left[ \left( \frac{t}{2} + \frac{d_0}{c_{conc}} \right) c_{conc} \right]^2 - \left( \frac{d_x}{2} \right)^2} \quad (4)$$

The wave speed for the pulse in air and concrete are determined based on values discussed in Section 2.1.2.

One important unknown is the wave speed in concrete,  $c_{air}$ , which is a function of the dielectric constant,  $\epsilon_r$  of the concrete. One idea is to take a scan in a lightly reinforced area and by holding a steel plate to the other side of the measurement to improve the amplitude of the reflected pulse. If the thickness is known, the dielectric constant can then be calculated. For real members, it can be difficult or impossible when dense reinforcing bar meshes are present. For this study, it was possible to calibrate this value based on the observed reflections, mainly from the geometry of the specimens.

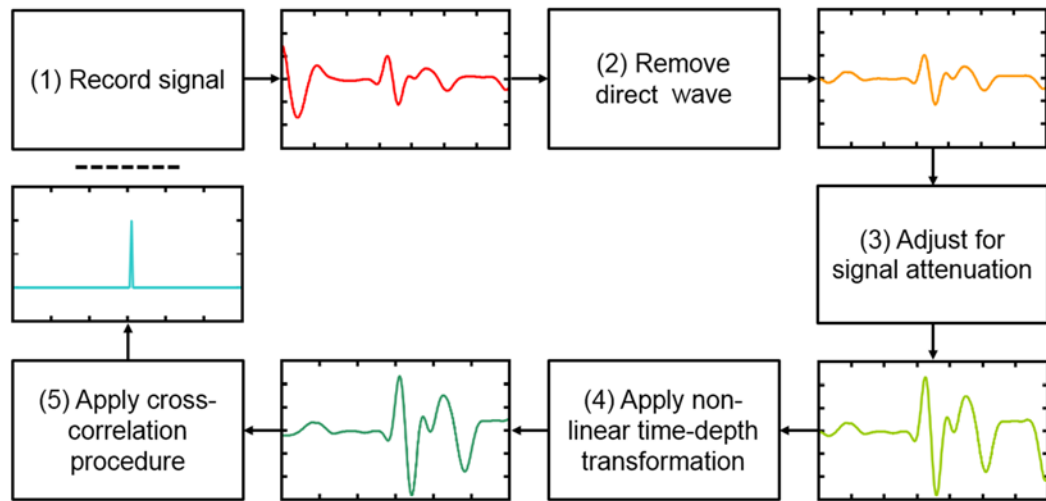


**Fig. 6.** Overview of proposed data processing steps illustrated on an A-scan.

Fig. 6 illustrates the proposed data processing steps shown for an A-scan. B-scans are created by lining up the recorded A-scans next to each other. To visualize B-scans effectively, a grey-scale contour representation was chosen with positive and negative values shown in white and black, respectively. Hence, reflections from steel and water should be represented by white, and air by black colors.

The proposed data processing steps are as follows:

- (1) Record signal: the raw data is collected using the hand-held GPR device introduced in Section 2.2.1.
- (2) Remove direct wave: The direct wave [see Fig. 5 (b)] traveling in the air gap (stand-off distance  $d_0$  between T and R) is removed by subtracting a reference A-scan taken without any reflectors.

- (3) Adjust for signal attenuation: the later portions of the signal are amplified to compensate for geometrical and material related amplitude attenuation by applying the function  $A_{adj}(i) = A_{GPR}(i) \left( \frac{i}{512} + 1 \right)^3$  to each A-scan. This function and the parameters were determined by trial and error to achieve reasonable B-scans (Step 4) and cross-correlation results (Step 5).
- (4) Apply non-linear time-depth transformation: depth values,  $d$  corresponding to total signal time,  $t$  are calculated according to Eq. 4.

An algorithm based on cross-correlation is applied to determine the exact location of the first reflected pulse corresponding to  $A_{GPR}$  in each A-scan. In essence, an assumed transmitted signal [Fig. 5 (a)] is cross-correlated with each preprocessed A-scan [Fig. 5 (b)] where the maximum of the cross-correlation function corresponds to the approximate pulse travel time, which then can be used to determine time,  $t$  (see Fig. 5). This process is run twice with positive and negative input signals to determine the polarity of the reflection amplitude. The exact time is then determined by searching for the actual maximum (or minimum) in the A-scan around that estimated location. This second step is necessary due to the fact that the reflected signals experience material dispersion (Lai et al. 2011), which influences the duration (and hence frequency) of the pulse, which in turn results in errors. The corresponding depth,  $d$  to that time is computed using Eq. 4 and shown in red or blue corresponding to a positive or negative reflection pulse, respectively. Finally, a filter is applied to reduce the amount noise due to erroneous predictions.

## 2.3 Laboratory Tests

A series of laboratory tests were performed to evaluate the accuracy and reliability of the proposed signal processing procedure using the hand-held GPR device.

### 2.3.1 Concrete Blocks

Basic laboratory tests on unreinforced concrete blocks with a thickness of 154 mm (6.06 in) were carried out to study the recorded signals. The blocks were made of a normal weight concrete with a target cylinder compressive strength of 31.0 MPa (4500 psi). An illustration of the test setup is shown in Fig. 7. Several different situations were created, and data recorded for analysis:

- Concrete–concrete: the concrete block was placed on top of a second concrete block with an air gap,  $a$  varying from 0 to 12.7 mm (0 to 0.5 in).

- Concrete–water–concrete: the concrete block was placed directly on top of a wetted second concrete block, i.e.,  $a \approx 0$ .
- Concrete–air: the concrete block was tested without anything behind it, i.e.,  $a = \infty$ .
- Concrete–steel: the concrete block was placed on top of a 50 mm (0.97 in) thick structural steel plate with an air gap,  $a$  varying from 0 to 12.7 mm (0 to 0.5 in).

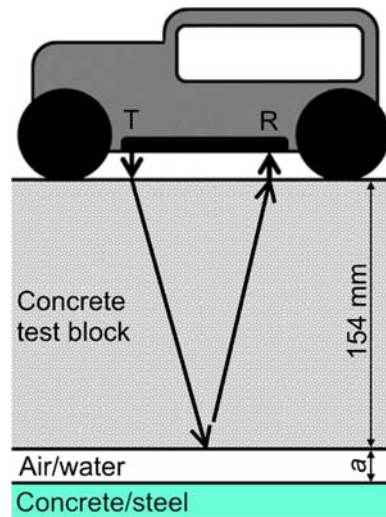


**Fig. 7.** Illustration of test setup for basic tests on unreinforced concrete block.

Fig. 8 shows selected A-scans from the concrete block tests. Fig. 8 (a) shows the received signals for three different scenarios: steel, air, and water as reflectors. The data processing steps used for this analysis were Steps 1, 2, and 4, employing a dielectric constant,  $\epsilon_r = 6.4$ . As can be observed, the polarity (positive and negative first pulse for steel/water and air, respectively) as well as the amplitudes (qualitatively judged) comply with theory as calculated using Eq. 2. In Fig. 8 (b) the concrete block was located on top of the steel plate. For this case, the amplitude of the reflected pulse remains approximately the same, but the pulse is aligned with the location of the steel plate. The slight decrease in reflected pulse amplitude is a result of the increased travel distance in the air gap. Fig. 8 (c) shows the scenario where the concrete block was located on top of another concrete block with a varying air gap. It can be observed that the first pulse is negative and approximately at the same location for all configurations indicating that the reflection occurs at the back wall of the concrete block. For the case where there is no concrete block, i.e.,  $a = \infty$ , a small time delay is present compared to the other signals. This could be due to the destructive interference between the signals reflected from the bottom surface of the first and the top surface of the second concrete block. Overall, the increasing air gap corresponds to an increasing reflection amplitude.

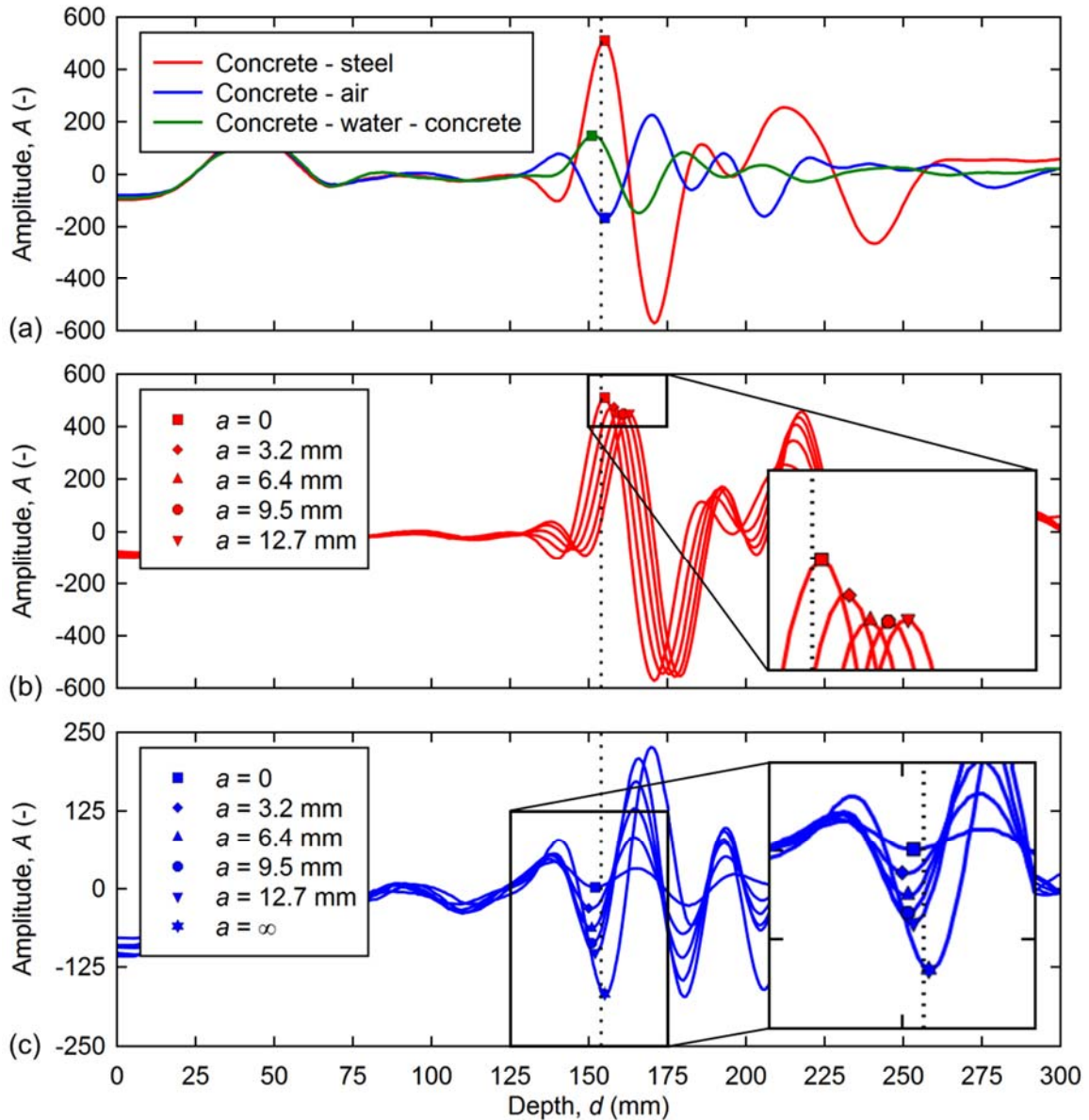


**Fig. 8.** Selected A-scans collected from concrete test block: (a) Different back wall materials, (b) concrete on steel with variable air gap, and (c) concrete on concrete with variable air gap. The vertical dotted line at  $d = 154$  mm (6.06 in) represents the thickness of the concrete test block. Relative dielectric constant,  $\epsilon_r = 6.4$ . Unit conversion example: 12.7 mm = 0.5 in.

### 2.3.2 Laboratory Bridge Mock-up Specimens

Three reinforced concrete mock-up bridge specimens were constructed in the laboratory to provide realistic means to evaluate the proposed signal processing procedure: Specimen 1 [Figs. 9 (a) and (b)] has variable concrete thicknesses and Specimen 2 [Fig. 9 (c)] represents a realistic concrete bridge deck with artificial delaminations and a section with stay-in-

place formwork. Specimen 3 was built to represent a realistic concrete bridge girder with varying rebar dimensions and concrete cover as well as two empty post-tensioning ducts. Fig. 9 (d) shows the overall geometry of the specimens. A normal weight concrete typical for bridge applications was used with a target cylinder compressive strength of 34.5 MPa (5000 psi). At the time the data for this study were collected, the specimens were approximately 3.5 years old and had been exposed to the weather in Newark, DE for one calendar year. For Specimens 1 and 2, the locations of the  $\varnothing$  13 mm (#4) reinforcing bars were estimated using an Eddy-current-based rebar locator. The reinforcing bars for Specimen 3 could be measured directly as the bars extend past the physical boundary of the specimen. The specimens were scanned on the top surface, except for Specimen 3, which was scanned on both sides. All specimens have a width of approximately 1000 mm (40 in). Note that Specimen 1 consists of two parts of approximately 500 mm (20 in) width with 1a and 1b having four discrete thicknesses and a smoothly varying thickness, respectively. To avoid interference of longitudinal rebars (oriented parallel to the scanning direction), they were first mapped using the same hand-held GPR device. The actual scans were then collected between two such bars.

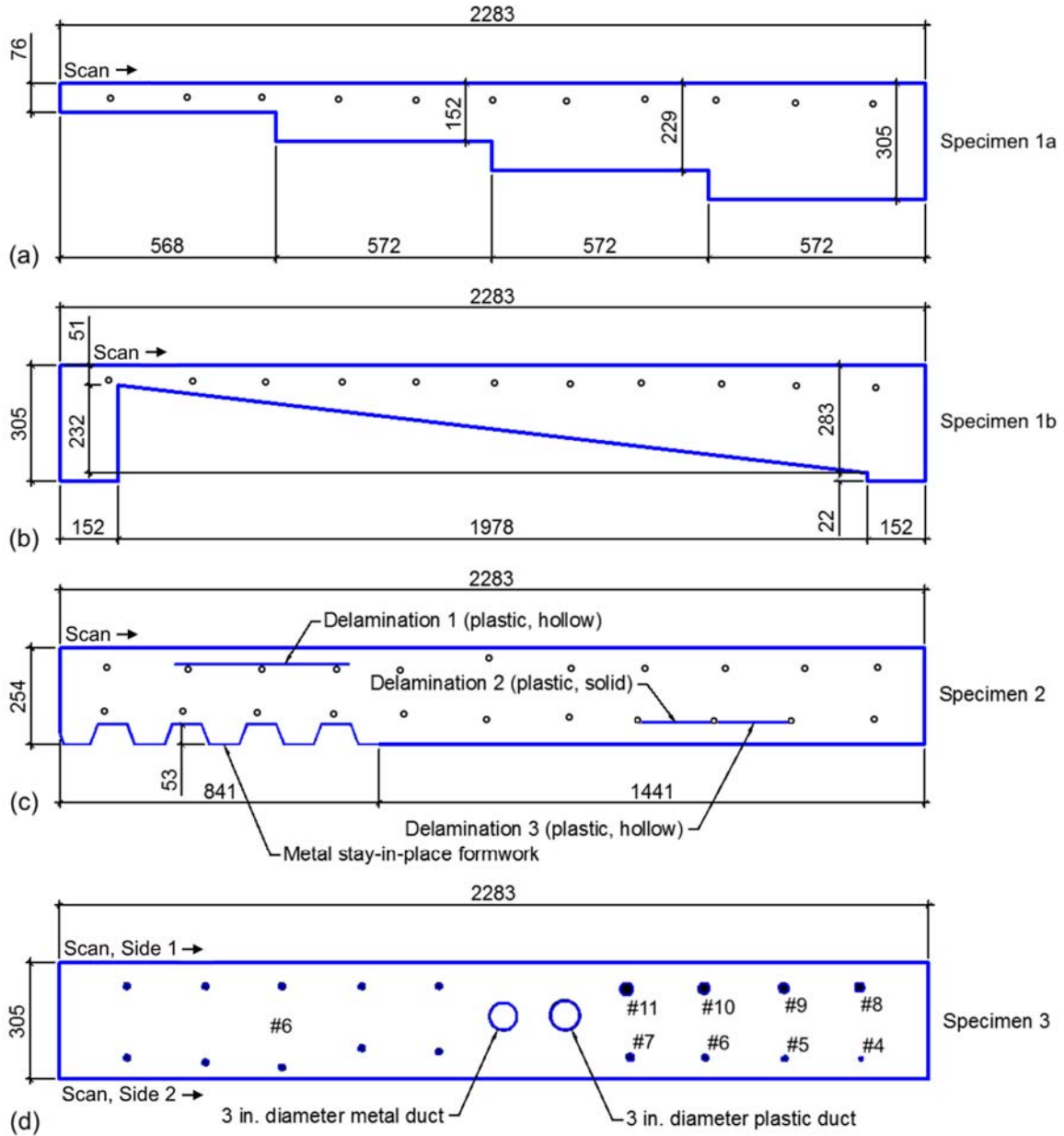


**Fig. 9.** Drawings of laboratory mock-up specimens: (a) and (b) lightly reinforced (top layer) specimens with variable thickness, (c) bridge deck specimen with artificial delaminations and stay-in-place formwork section, and (d) bridge girder specimen with variable rebar dimensions and concrete cover and two empty post-tensioning ducts. All dimensions are in (mm). Unit conversion example: 305 mm = 12 in.

Figs. 10 to 14 show the analysis results for the proposed data processing procedure: (a) shows the reflected pulse amplitude,  $A_{GPR}$  from the reinforcing bars extracted from an unamplified version of the B-scan data, i.e. by using data processing Steps 1 and 2. A traditional B-scan created by applying data processing Steps 1 through 4 is shown in (b)

and the cross-correlation result achieved by applying data processing Steps 1 through 5 is illustrated in (c). Red and blue dots correspond to positive (e.g., steel rebar) and negative (e.g., delamination or geometric boundary), respectively. The actual specimen outline is also shown for reference in (b) and (c). Additionally, for round reflectors (= rebars and ducts) resulting in a hyperbola in the B-scan, the automatically picked point corresponding to the top of the rebar corresponding to the concrete cover is indicated by a red ‘▼’ in (c).

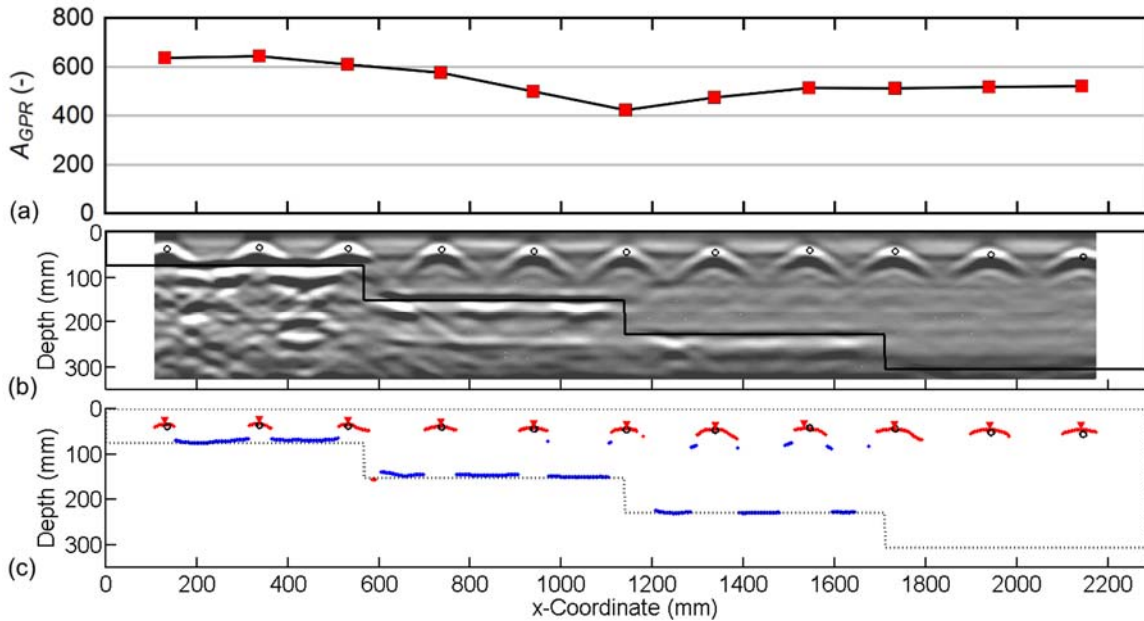


**Fig. 10.** (a) Reflected pulse amplitude from rebar, (b) B-scan, and (c) cross-correlation results for Specimen 1a. Relative dielectric constant,  $\epsilon_r = 8.0$ . Unit conversion example: 305 mm = 12 in.

The reflected pulse amplitudes for Specimen 1a [dimensions see Fig. 9 (a)] are approximately between 400 and 600 [Fig. 10 (a)]. The B-scan [Fig. 10 (b)] clearly shows the steel rebars as well as the back walls up to a thickness of 229 mm (9 in) representing the thickness of the specimen. The cross-correlation results [Fig. 10 (c)] predict the location and polarity accurately. It can be observed that the back walls are not predicted continuously. The reason for this is that only the first clear reflection was included in data processing Step 5. The results for Specimen 1b [dimensions see Fig. 9 (b)] are very similar (Fig. 11). Also, the reflected pulse amplitudes in the regions where the specimen is less than approximately 100 mm (4 in) are notably higher.

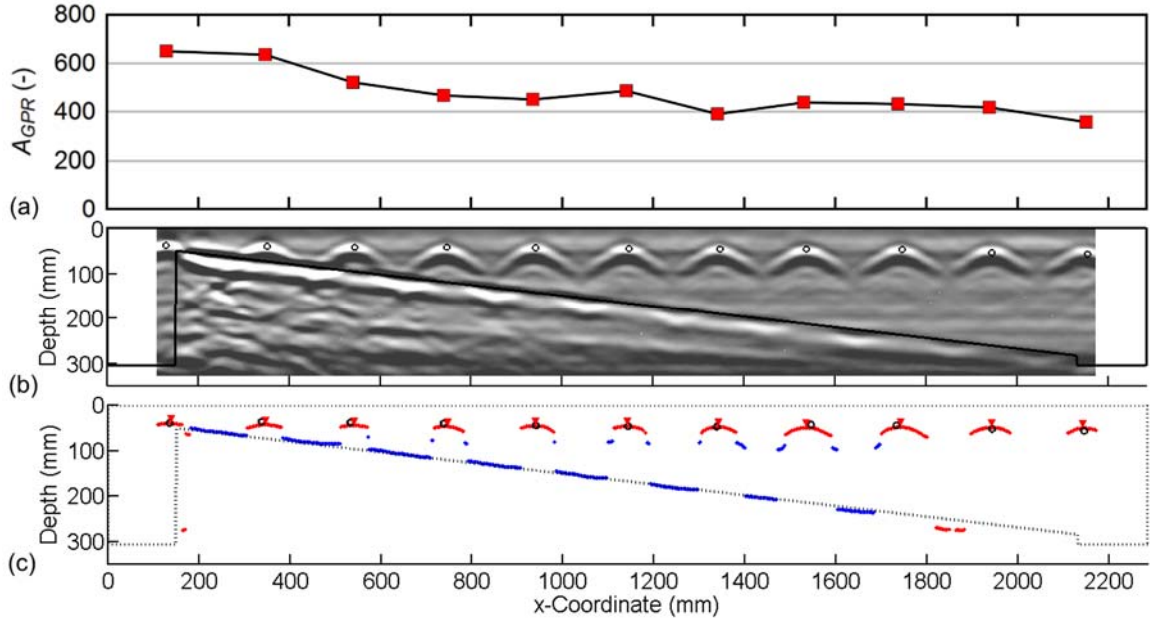


**Fig. 11.** (a) Reflected pulse amplitude from rebar, (b) B-scan, and (c) cross-correlation results for Specimen 1b. Relative dielectric constant,  $\epsilon_r = 8.0$ . Unit conversion example: 305 mm = 12 in.

In Fig. 12, the results for Specimen 2, the bridge deck mock-up specimen [dimensions shown in Fig. 9 (c)] are presented. The reflected pulse amplitudes [Fig. 12 (a)] show more scatter as they lie between approximately 200 and 600. It can be observed that the shallow delamination is clearly visible in the B-scan [Fig. 12 (b)] and is also correctly predicted, with respect to both location as well as polarity, using the herein proposed cross-correlation procedure, although not across the entire length [Fig. 12 (c)]. The deep delamination, however, is identified in two spots to be steel. The reason for this was that a steel wire was used to hold the delamination in place at that location. As a result, no attempts are made to make any conclusions with respect to this delamination. The stay-in-place formwork is also picked up but not in its entirety because it is on the bottom surface and sheltered by the two reinforcement layers. The only point that was clearly identified is the top right corner of each rib resulting in the start of hyperbola.

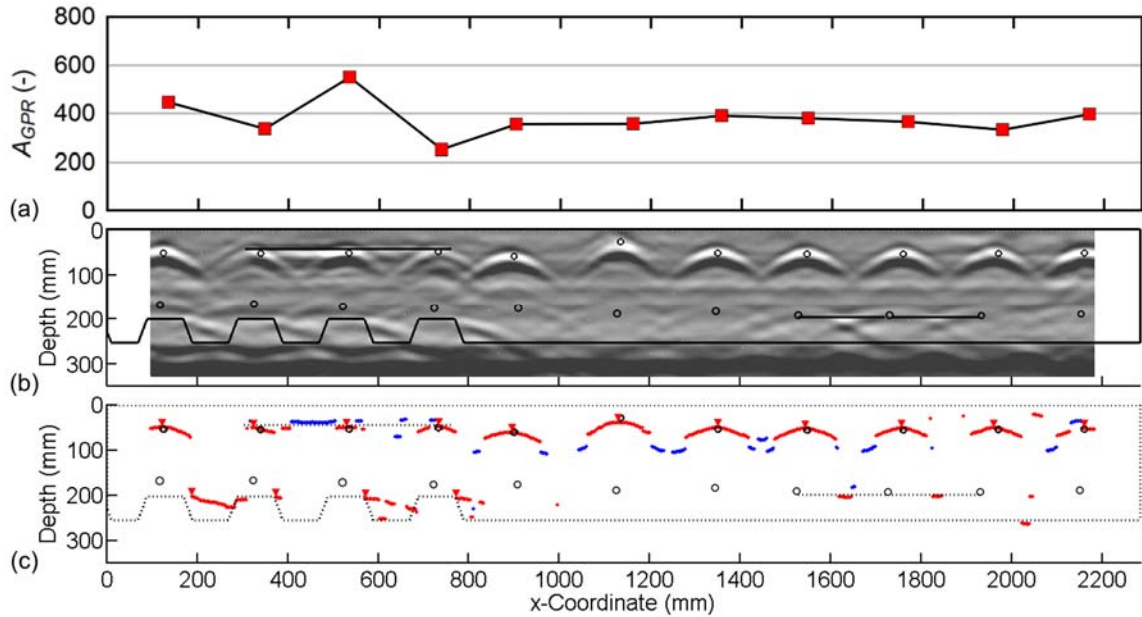


**Fig. 12.** (a) Reflected pulse amplitudes from rebars, (b) B-scan, and (c) cross-correlation results for Specimen 2, Side 1. Relative dielectric constant,  $\epsilon_r = 9.0$ . Unit conversion example: 305 mm = 12 in.

Figs. 13 and 14 show the results for Specimen 3, the bridge girder mock-up specimen [dimensions see Fig. 9 (d)]. As can be observed, the locations as well as polarity of the rebars and ducts - the empty plastic duct is shown in blue - are correctly predicted by the proposed cross-correlation procedure [Figs. 13 and 14 (c)]. There is also a strong correlation between the #6 steel rebars and the depth [Fig. 14 (a)]. The size of the rebars having a constant depth is present but not very strong [Fig. 13 (a) right and Fig. 14 (a) left]. Relationships between estimated and actual rebar depth as well as reflected pulse amplitude and depth are investigated in greater detail in Fig. 16.

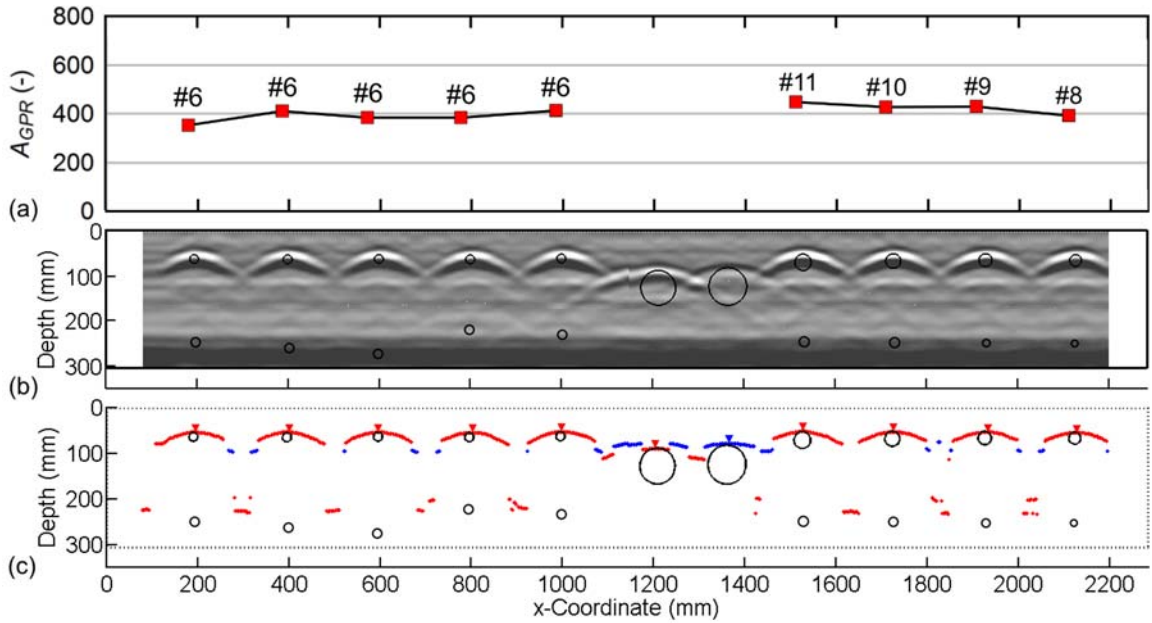


**Fig. 13.** (a) Reflected pulse amplitudes from rebars, (b) B-scan, and (c) cross-correlation results for Specimen 3, Side 1. Relative dielectric constant,  $\epsilon_r = 10.5$ . Unit conversion example: 305 mm = 12 in.

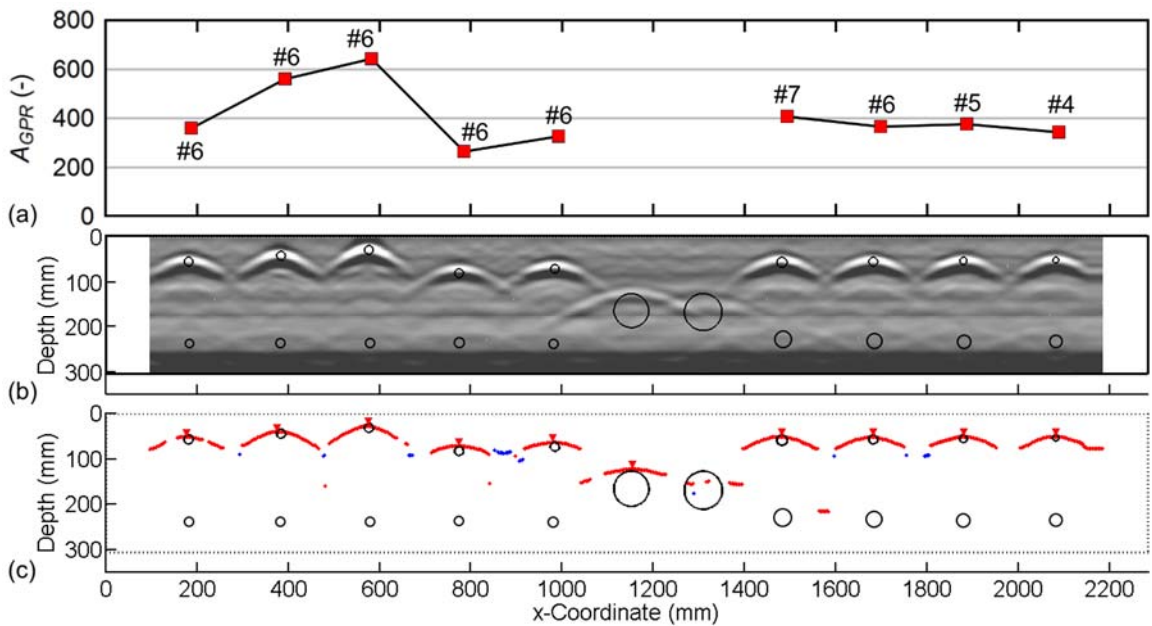


**Fig. 14.** (a) Reflected pulse amplitudes from rebars, (b) B-scan, and (c) cross-correlation results for Specimen 3, Side 2. Relative dielectric constant,  $\epsilon_r = 10.5$ . Unit conversion example: 305 mm = 12 in.

In Fig. 15, the correlation between estimated and actual reflector depth are compared for all three specimens using the points predicted from the cross-correlation approach [shown in Figs. 10 to 14 (c)]. The data in red and blue represent reflections from steel reflectors and concrete back walls, respectively. For the steel rebars, only one point was automatically picked (smallest depth corresponding to concrete cover) and for the specimen thickness, the entire series of points was picked and is included. It can be observed that the depth of reflectors in concrete can be estimated with reasonable accuracy [16 mm (0.63 in) at the 95% prediction limits] using the proposed analysis procedure and if the correct relative dielectric constants are used.

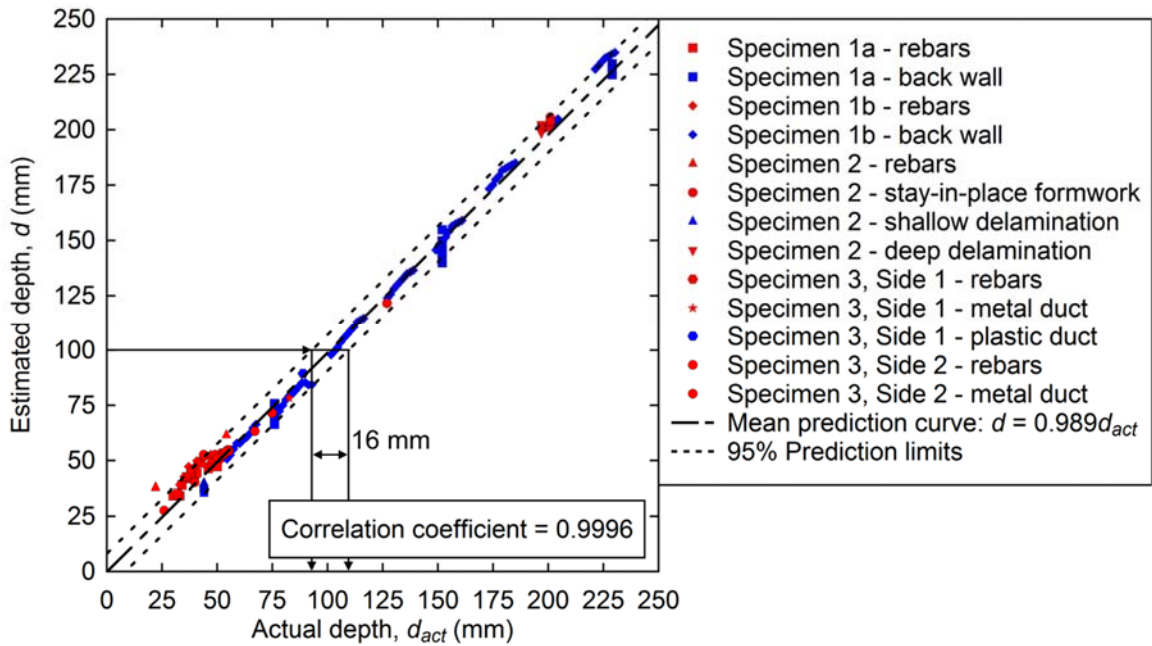


**Fig. 15.** Correlation of actual vs. observed depth for all laboratory mock-up specimens. The dashed-dotted and dotted lines represent mean and 95% prediction limits, respectively. Unit conversion example: 250 mm = 9.84 in.

Fig. 16 shows the correlation between reflected pulse amplitudes and rebar depth for all three laboratory specimens. Fig. 16 (a) shows all data with an exponential curve fit and 95% prediction and confidence limits. In Fig. 16 (b), only the results from Specimen 3 are shown. It can be observed that there is a very strong correlation between rebar depth (or: concrete cover) and reflected pulse amplitude. Additionally, a trend for larger rebars to create a larger reflected pulse amplitude can be observed but due to significant scatter it is not recommended that this relationship is used to predict reflector depth.

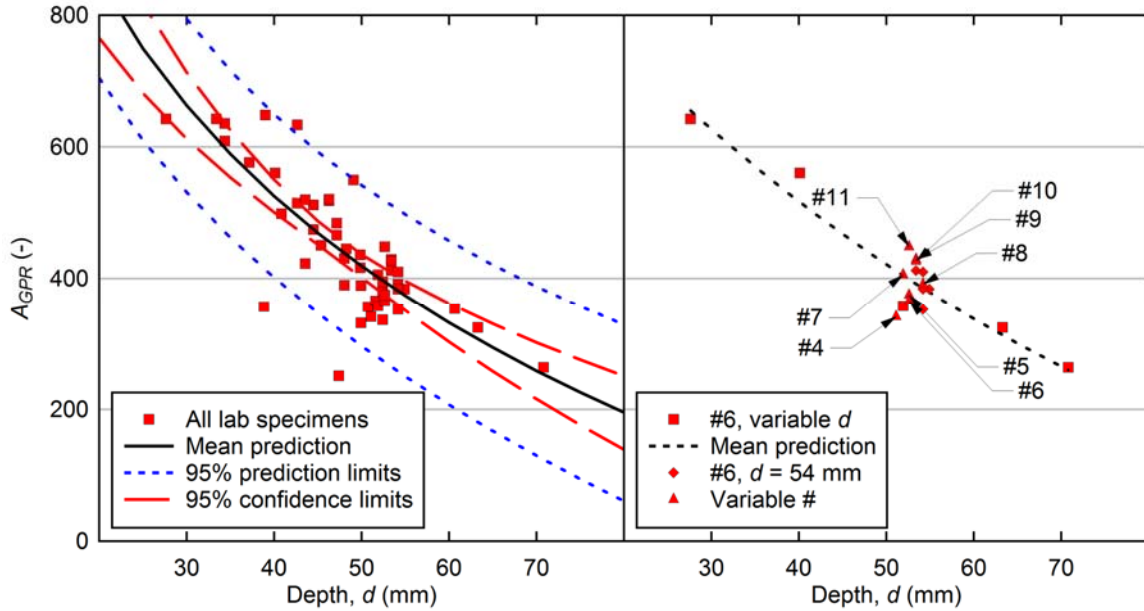


**Fig. 16.** Reflected pulse amplitudes from rebar vs. depth for (a) all three lab specimens and (b) for #6 rebars in Specimen 3. Unit conversion example: 70 mm = 2.76 in.

## 2.4 Summary and Conclusions

In this research, a consistent approach to process and interpret data collected from concrete members using a hand-held GPR device is presented. A series of laboratory experiments was conducted to evaluate the detection capabilities using this device and the proposed approach. The following conclusions can be drawn:

- It was possible to distinguish reflections from air, water, or steel through 154 mm (6.06 in) of unreinforced concrete by their polarity and amplitude.
- It was possible to detect an air gap of 3.2 mm (0.126 in) between two 154 mm (6.06 in) thick unreinforced concrete blocks.
- The depth of rebars perpendicular to the scanning direction could be detected reliably over a range of approximately 25 mm to 200 mm (1 to 8 in).
- The thickness of Specimen 1a and b could be estimated accurately. This was possible because there was only one layer of top reinforcing bars spaced at approximately 200 mm (8 in).
- The proposed cross-correlation methodology was able to automatically and accurately map reflectors such as reinforcing bars and geometric boundaries and detect their polarity.
- The embedded artificial shallow delamination in Specimen 2 was correctly identified.
- The depth of reflectors could be located with an accuracy of 16 mm (0.63 in) at the 95% prediction limits.

- A trend between reflected pulse amplitude and reflector depth can be observed but scatter is significant, i.e., this relationship should not be used to predict reflector depth.

A limitation of the herein proposed methodology is that it is only able to detect the first clear reflection in each GPR signal. Including additional reflections could be included, although this may be challenging due to signal attenuation and noise. Further research will include validation of the proposed methodology on real concrete bridge decks.

## **2.5 Acknowledgements**

Special thanks go to the Delaware Department of Transportation (DelDOT) for funding this research, which resulted in an M.S. Thesis (Clem 2013). Furthermore, the Summer Scholars Program from the University of Delaware Undergraduate Research Program supported the third author of Clem et al. (2015) in the summer of 2013. Final thanks go to Francisco Romero from Romero NDT & E, LLC for his valuable insight and comments regarding the GPR measurements.

## **2.6 Field Application Example**

Nine GPR B-scans collected on the in-service bridge (Deck #3) introduced in Section 3.4.1 are shown in Fig. 17. This deck exhibited significant deterioration due to the harsh environment it had been experiencing. A prior visual inspection along with hammer sounding revealed delaminated areas, which are marked as white lines. Multiple areas of cover loss existed that had been filled with bituminous asphalt. Those obvious areas of deterioration, i.e., areas (2), (4), (9), (11), (19), (20), (23), (26), (28), and (30), are not further discussed. Some locations where the rebar reflections are missing or heavily distorted coincide with the presence of delaminations, as they were found by hammer sounding, i.e., areas (1), (3), (6), (17), (23), and (29). Ambiguous or missed areas of delamination include: (5), (7), (8), (10), (12) through (16), (18), (21), (22), (24), (25), and (27). Variations in the brightness (or strength) of the rebar reflections can be related to deterioration (ASTM 2008). This approach is not discussed here because it requires a different type of GPR equipment. The reader is referred to Celaya et al. (2014) where measurements from this same bridge are reported and discussed.

Overall, the GPR B-scans taken by the hand-held instrument provide useful information regarding the location and depth of rebars and can in some cases help to identify delaminations. Factors that affect the detectability are rebar condition (e.g., level of corrosion), thickness and status of delamination crack, e.g., whether it is dry or saturated with water.

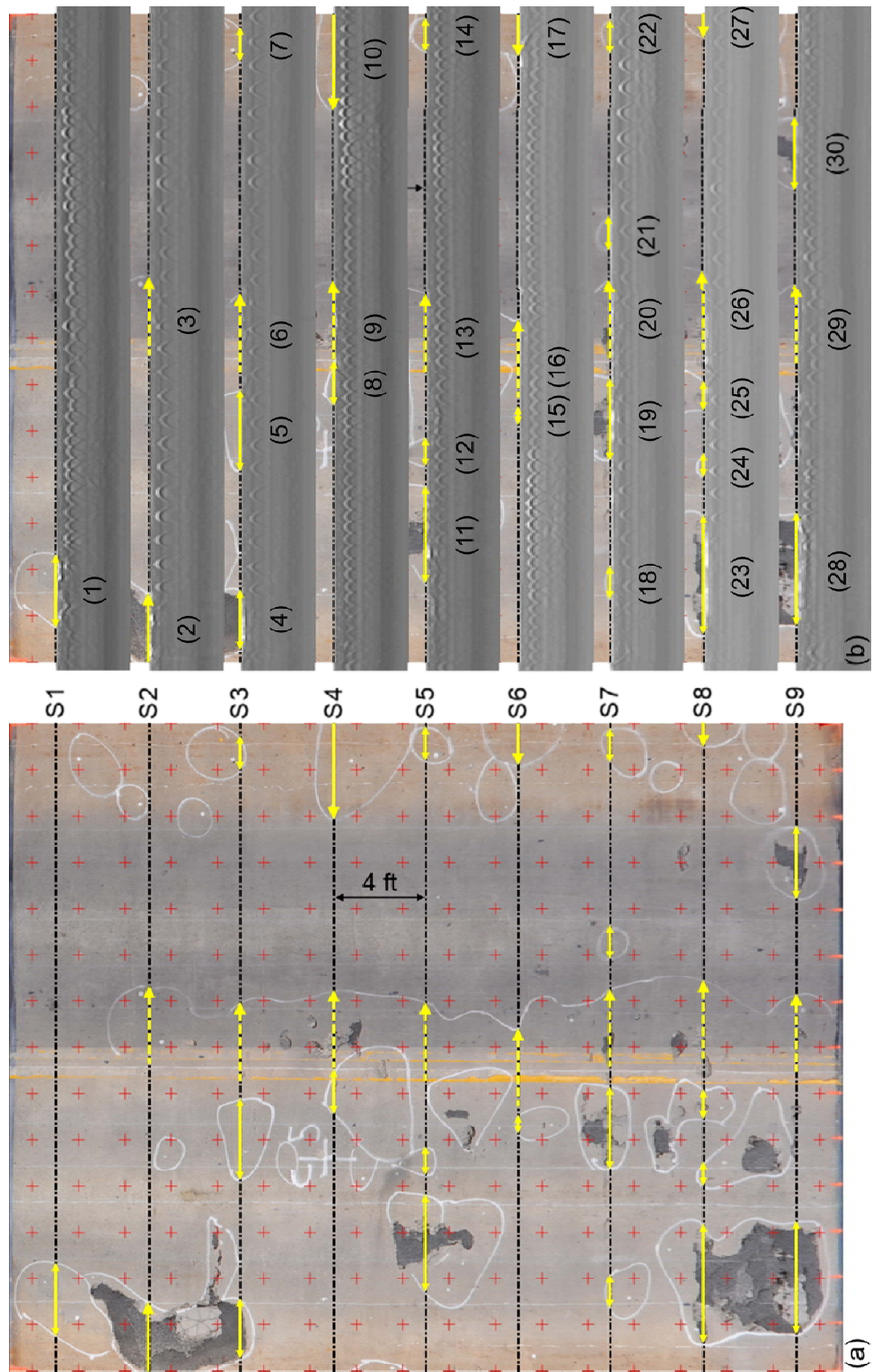


**Fig. 17.** GPR results for Deck #3: (a) Plan view of deck and (b) B-scans. Yellow arrows mark lines on the scans that had been determined as delaminated by hammer sounding.

Red + mark the locations for which IR measurements were performed, which are discussed in Chapter 3. Unit conversion: 4 ft = 1.22 m.

### 3 IMPULSE RESPONSE TESTING

The content of Sections 3.1 through 3.7 is based on the following journal article:

Hafiz, A., Schumacher, T., and Raad, A. (2022). A Self-Referencing Non-Destructive Test Method to Detect Damage in Reinforced Concrete Bridge Decks Using Nonlinear Vibration Response Characteristics. *Construction and Building Materials*. Vol. 318, Article 125924. DOI: <https://doi.org/10.1016/j.conbuildmat.2021.125924>.

#### 3.1 Background and Motivation

Highway infrastructure in the United States and around the world experience degradation due to environmental conditions and increasing traffic volume. Additionally, damage is caused by degradation of structural materials due to aging. The corrosion of steel bars and resulting gradual degradation of the concrete are the most common causes of damage in reinforced concrete structures (NCHRP 2004). Accordingly, bridge engineers are typically concerned about four primary damage mechanisms: steel reinforcing bar (or rebar) corrosion, delamination, vertical cracks, and concrete degradation (Gucunski et al. 2013). Delaminations in concrete bridge decks, which are the focus of this research, are an advanced form of damage in reinforced concrete bridge decks resulting from advanced corrosion of the embedded steel rebar and are initiated by the presence of cracks in the concrete and sufficient moisture. The rebars expand due to corrosion, leading to cracking and subsurface fracture planes within the concrete. With advancing corrosion, delaminations can progress to open spalls.

To date, many non-destructive test (NDT) methods have been developed to detect deterioration in concrete bridge decks such as delaminations (Scott et al. 2003, Arndt et al. 2011, Zhang et al. 2012, Gucunski et al. 2013, Sun et al. 2018, Garrett 2019). An ultrasonic stress pulse is used in techniques aiming to initiate high-frequency stress waves, which include impact echo (IE) and ultrasonic echo (UE) testing (Sansalone and Streett 1997, Kee et al. 2012, Zhang et al. 2012, Shokouhi et al. 2014, Scherr and Grosse 2021). On the other hand, low-frequency dynamic response characteristics are used in impulse response (IR) testing (Davis 2003). In the latter method, specific characteristics of the dynamic response to a given hammer impact are evaluated to detect delaminations among other degradations. IR testing is based on a hammer impact resulting in a low strain stress wave and vibrations and it has been primarily used for pile integrity testing (Davis and Robertson 1975). While the methodology of this test has not changed since its popularization in the 1970s, application to other types of concrete members has increased notably (Davis 2003,

Davis and Germann Petersen 2003, Sajid and Chouinard 2019). ASTM Standard C1740 provides guidance for evaluating the condition of concrete plates such as bridge decks using the IR method (ASTM 2016). In IR testing, an instrumented hammer is struck against the concrete surface to generate local vibrations, and the dynamic response is measured at a nearby location using a geophone or accelerometer. The frequency response function (FRF) is obtained by dividing the dynamic response by the impact force, where both signals are expressed in the frequency domain. The typical frequency range used to evaluate the condition of a concrete slab is 0 to 1 kHz (ASTM 2016). Several parameters are computed from the FRF, referred to as mobility plot, that are used as empirical indicators of damage. For concrete bridge deck condition assessment, all available NDT technologies have limitations to identify certain types of defects (Abdelkhalek and Zayed 2020). One of the limitations of the IR method is that it cannot detect defects with a large depth-to-size ratio (Lin et al. 2021). Moreover, limitations in detecting delaminations of a certain size appear to be related to the fixed frequency limit prescribed by the ASTM standard (Clem et al. 2013). Finally, the method may not be sensitive to early stages of damage because it solely relies on linear response characteristics.

In structural dynamics, modal analysis is the most popular approach for performing linear-elastic structural system identification, where the modal parameters, i.e., natural vibration frequencies, mode shapes, and damping ratio, can be extracted and monitored over time (Kerschen et al. 2006, Farrar and Worden 2013). Since these parameters are a function of the structural and material properties, they can be related to the initiation and propagation of damage (Doebling et al. 1998). Samman and Biswas (1994) presented waveform-recognition techniques to detect damage in bridges and they applied these techniques under both laboratory and real-world conditions by detecting damage in a laboratory-sized bridge and a highway bridge. These techniques depend on a comparison between two dynamic signatures: one from an intact (= reference) state and the other from a state with a certain level of damage. Zhou et al. (2007) utilized vibration-based damage detection (VBDD) methods to detect and localize low levels of damage in the deck of a two-girder, simply-supported bridge. They conducted their study using laboratory-based experimental and finite element analysis. The methods evaluated included the mode shape curvature method, the change in flexibility method, the damage index method, the change in uniform flexibility curvature method, and the change in mode shape method. They concluded that VBDD methods have excellent potential as structural health-monitoring tools for bridge decks. However, these methods require extracting the mode shapes, a process requiring multiple sensors. Additionally, there is difficulty in extracting the mode shapes for bridge decks in the field (Salawu and Williams 1995, Bien et al. 2002) because the excitation

forces are required to have sufficiently large amplitudes (Bien et al. 2002). Kee et al. (Kee and Gucunski 2016) used impact-echo (IE) testing in order to improve the interpretation of local flexural vibration modes of delaminated areas in concrete bridge decks. This approach was more accurate than conventional binary images for detecting the areal sizes of shallow delaminations. On the other hand, for deep delaminations, the conventional IE approach was more accurate (Kee and Gucunski 2016). Finally, there are two challenges in using modal analysis methods for damage detection: first, it requires the dynamic response for the reference case, which is unavailable in most cases. Second, temperature variations can have a significant effect on the frequency response of the structure (Zhou et al. 2011), and there might be significant difficulty in distinguishing between the effects of temperature and damage.

Fundamentally, if a structural system fails to follow the principle of superposition, i.e., its response deviates from linearity, then it can be considered nonlinear (Ewins 1995), and traditional linear-elastic modal analysis cannot be used to analyze the dynamic response. In reality, most structural systems exhibit a certain level of nonlinear behavior (Lin 1990). The sources of nonlinearity can be summarized as (Farrar and Worden 2013): (1) Geometric nonlinearity, when the structure exhibits large displacements, (2) material nonlinearity, when a material exhibits a nonlinear stress-strain response, (3) nonlinear boundary conditions, where imperfect boundary conditions result in a nonlinear vibration response, (4) damage, for example cracking, and (5) energy dissipation due to damping. This last phenomenon is to date not fully understood. According to Samman and Biswas (Samman and Biswas 1994), the identification of nonlinear behavior of a structural system includes three steps. The first step is “Detection,” where the existence of nonlinearity in structural behavior is determined. “Characterization” is the second step, where the source and location of the nonlinearity is investigated, and its behavior established. The final step is “Parameter estimation.” In this step, the coefficients of the nonlinearity are estimated, and their uncertainty quantified. There are many identification methods that have been established in the preceding three decades, such as the restoring force surface method and nonlinear autoregressive moving average model with exogenous inputs (NARMAX) method (Kerschen et al. 2006, Noel and Kerschen 2017). Nonlinearity is important in damage detection for cases where damage changes the behavior of the structural form (initially) from linear to nonlinear (Lin 1990). Underwood et al. (2015) investigated using nonlinear behavior for detecting and locating subsurface damage in composite materials by comparing the FRFs for different input force amplitudes. Idriss et al. (2015) found that nonlinear vibration parameters are much more sensitive to debonding damage in sandwich beams than linear vibration parameters. Zhao et al. (2015) presented a new transmissibility

analysis method for the detection and location of damage using the characteristics of nonlinear vibrations of structural multi-degree-of-freedom (MDF) systems.

This literature review reveals an opportunity to improve the sensitivity of the established IR test method to detect delaminations in concrete bridge decks early on. The objective of this study was thus to develop and evaluate a highly sensitive yet simple NDT test method to detect damage such as delaminations in reinforced concrete bridge decks. Unlike traditional vibration-based methods, the method discussed herein is self-referencing, i.e., it does not require a reference measurement of the undamaged state for comparison. Using the impulse response (IR) test procedure, the collected data is analyzed in a manner that enables us to detect damage based on deviation from linearity, following what was originally proposed by Ewins (1995), i.e., by comparing the frequency response functions (FRF) due to impacts of varying amplitude. The significance of the proposed method lies in its availability, simplicity, cost-effectiveness, and that its application could be extended to other members.

### **3.2 Test Methodology**

The proposed method is based on the vibration response of a reinforced concrete bridge deck and produces a nonlinear vibration index (NVI) for each test point on the member. The same instruments and general test procedure used for impulse response (IR) testing and vibration-based methods apply: An instrumented hammer is used to create an impact at a specific test point and the vibration response at a nearby location is measured with an accelerometer (see Fig. 18). For an introduction to IR testing and traditional IR parameters used to characterize damage in concrete plates, the reader is referred to Clem (2013). The proposed method requires applying at least two impact forces with different amplitudes for each test point and measuring their vibration responses separately. The basic concept is that for a test point on an ideal undamaged linear-elastic structural system, varying the amplitude of the impact force does not result in a change in the FRF. On the other hand, a test point on a system that contains damage exhibits nonlinear characteristics, which result in different FRFs for impact forces of different amplitude. The frequency ranges of the FRFs need to be within the linear operating range of the measurement system.

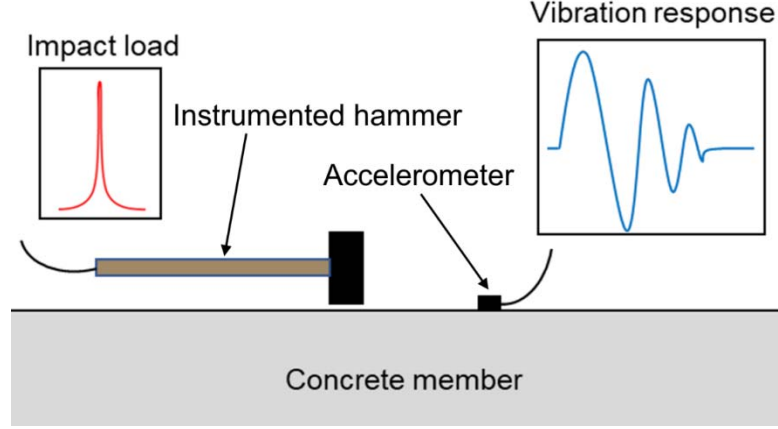


**Fig. 18.** Illustration of test setup used in this study.

A parameter describing the nonlinearity effect, or deviation from linearity, can be computed in multiple ways, see e.g., Idriss et al. (2015), Zhao et al. (2015) and Liu et al. (2017). Typically, the correlation coefficient or root mean square are used. Assuming two different impact forces (e.g., soft and strong), the proposed NVI is computed for each test point as follows:

$$FRF = H(f) = \frac{Y(f)}{X(f)} = \frac{G_{xy}(f)}{G_{xx}(f)} \quad (5)$$

$$COV(H_0, H_i)(f) = \frac{1}{f-1} \sum_{j=1}^f (H_0 - \mu_{H_0})(H_i - \mu_{H_i}) \quad (6)$$

$$\rho_{H_0, H_i}(f) = \rho(f) = \frac{COV(H_0, H_i)(f)}{\sigma_{H_0} \sigma_{H_i}} = \frac{\sigma_{H_0, H_i}}{\sigma_{H_0} \sigma_{H_i}} \quad (7)$$

$$R^2(f) = \rho(f)^2 \quad (8)$$

$$NVI = \frac{\sum_{f_1}^{f_2} R^2(f)}{f_2 - f_1} \quad (9)$$

where  $Y(f)$  and  $X(f)$  are the frequency domain representations of the measured vibration response and the impact force, respectively, and  $H_0$  and  $H_i$  are the FRFs associated with two impact forces having different amplitudes. In this study, the FRF associated with the lowest force of a set of measurements from a particular test point was assigned to  $H_0$ , representing the reference case.  $COV(H_0, H_i)$  is the covariance between  $H_0$  and  $H_i$ , and  $\mu$  indicates mean values.  $\rho$  is the correlation coefficient,  $f_1$  and  $f_2$  are the lower and upper limits of a selected frequency range, respectively.  $G_{xy}$  is the cross spectrum between the measured vibration response and the impact force and  $G_{xx}$  is the auto spectrum of the measured impact force. NVI is the proposed nonlinear vibration index and a scalar between

0 and 1, indicating the level of nonlinearity in the structural system under evaluation. When  $H_0 = H_i$ , then  $NVI = 1$ , implying the structural system behaves linearly; otherwise, the FRFs are different, which implies that the structural system exhibits a certain level of nonlinearity.

In the herein proposed method, a test point on a bridge deck without damage is assumed to represent an ideal linear-elastic structural system, i.e., the FRF does not change with an increase in the amplitude of the impact force. This is illustrated in Fig. 19, where the FRFs of four impact forces with increasing amplitude [Fig. 19 (a)] are shown for test point A1 [see Fig. 26 (a)] on the tested bridge deck (introduced in Section 3.4.1). From Fig. 19 (b), it can be observed that increasing the applied impact force, even doubling it, does not result in significant visible differences between the FRFs, indicating system linearity, which in turn implies that no damage is present in the system. The hypothesis is that if any area of a bridge deck deviates from linearity, some type and level damage can be assumed to be present. The observed nonlinearity is assumed to be caused by cracking and crack boundary interaction. Note that all other potential sources of nonlinearity must be controlled, i.e., minimized (see Section 3.4.3). Also, the selected frequency range ( $f_1 = 225$  to  $f_2 = 500$  Hz) was determined by trial and error and is application dependent. More details are provided in Section 3.4.2.

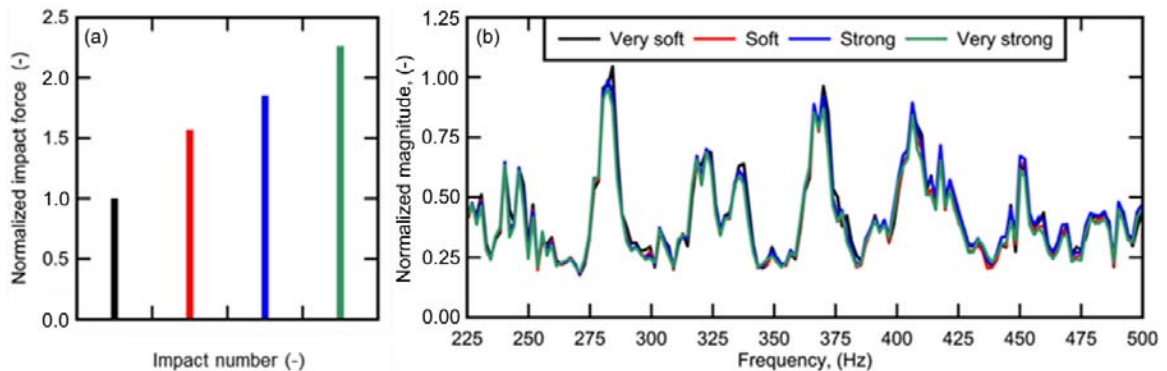


**Fig. 19.** Sample FRFs for test point A1 [see Fig. 24 (a)] on the selected bridge deck.

Fig. 20 shows a sample of the coefficient of determination,  $R^2$  as a function of frequency. This coefficient was determined by comparing the FRFs of the very soft and very strong impact forces shown in Fig. 19 (b). Finally, the normalized area under the coefficient of determination-frequency curve represents the NVI, which for this case is 0.98. This value confirms that the system shows a very high degree of linearity at this test point, which was consistent with visual inspection results.

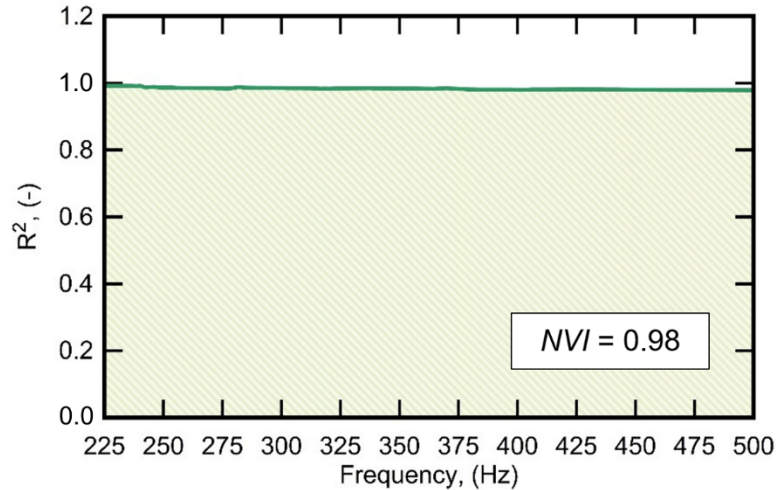


**Fig. 20.** Sample  $R^2$  -frequency relationship for two FRFs [very soft and very strong from test point A1, see Fig. 26 (a)] vs. frequency and corresponding NVI.

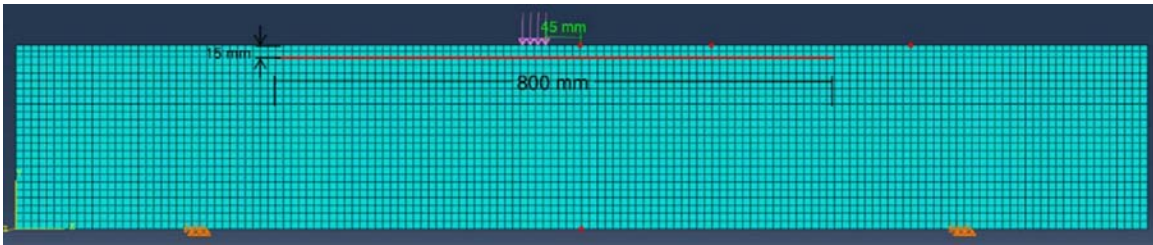
Unless otherwise noted, computations were performed in MATLAB (Mathworks 2020) and plots generated in DPlot (Hyde 2014). Regressions and statistical metrics were computed using STATGRAPHICS (Centurion 2020).

### 3.3 Numerical Study

#### 3.3.1 Modeling

A plane strain 2D finite element (FE) model was created to simulate the dynamic response of concrete bridge decks with and without delamination theoretically. The objective was to study the effect of a delamination on the dynamic response and whether it causes a nonlinear response. To that end, depth and width of the delamination were selected based on trial and error to prove that the idea works and not necessarily to represent an actual scenario. The bridge deck was modeled as a simply-supported 2D beam using ABAQUS (Dassault Systemes 2012) and guided by previous work reported in (Clem et al. 2013). The model was created using quadrilateral elements, as shown in Fig. 21. The span length is 1.00 m (39.4 in) and the depth is 240 mm (9.45 in). The material properties assigned to the deck are normal-weight concrete with a modulus of elasticity,  $E_c = 23,520$  MPa (3,410 ksi) and a mass density,  $\rho = 2400$  kg/m<sup>3</sup> (150 lb/ft<sup>3</sup>). An impact force modeled after a typical one observed in the field measurements (see Section 3.4) was applied as a distributed time-varying force over a length of 40 mm (1.58 in), which corresponds to the diameter of the hammer tip. The forcing function followed a sine (half of a complete cycle) with a duration of 1.8 ms. The acceleration response was measured at a point located 45 mm (1.77 in) from the applied impact force.

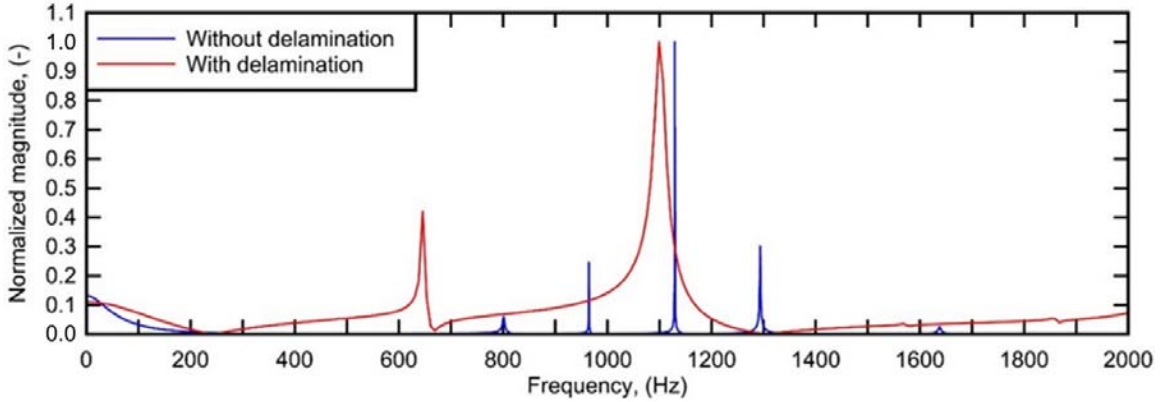
Two separate beam models were created: Model 1 refers to the concrete beam without delaminations, i.e., the intact (or reference) beam. Model 2 has the same geometry as Model 1 beam but with a delamination, which was modeled as a gap with the following dimensions: Width = 0.5 mm (0.02 in), length = 800 mm (31.5 in), located about the center of the beam at a depth of 15 mm (0.59 in) (see Fig. 21). To capture interactions of the delamination boundaries during vibration, these surfaces were modeled as contact elements. In both models, eight impact forces were applied to each of the beams where the peak value of the impact force varied from 0.5 to 15 kN (0.112 to 3.37 kip). This range was selected based on the actual forces employed in the field (see Section 3.4). Note that impact forces reported herein are total force and equivalent distributed forces as applied to the FE models can be calculated as force/0.04 m. A dynamic explicit step routine with a time step of 10  $\mu$ s and a total simulation time of 1 s was used. The dynamic response of all 16 simulations was analyzed and is discussed in the following subsection.



**Fig. 21.** Illustration of the 2D finite element (FE) model for Model 2. The red line indicates the delamination (gap). The red point at the surface indicates the acceleration measurement point. The purple arrows indicate the distributed force applied on the deck.

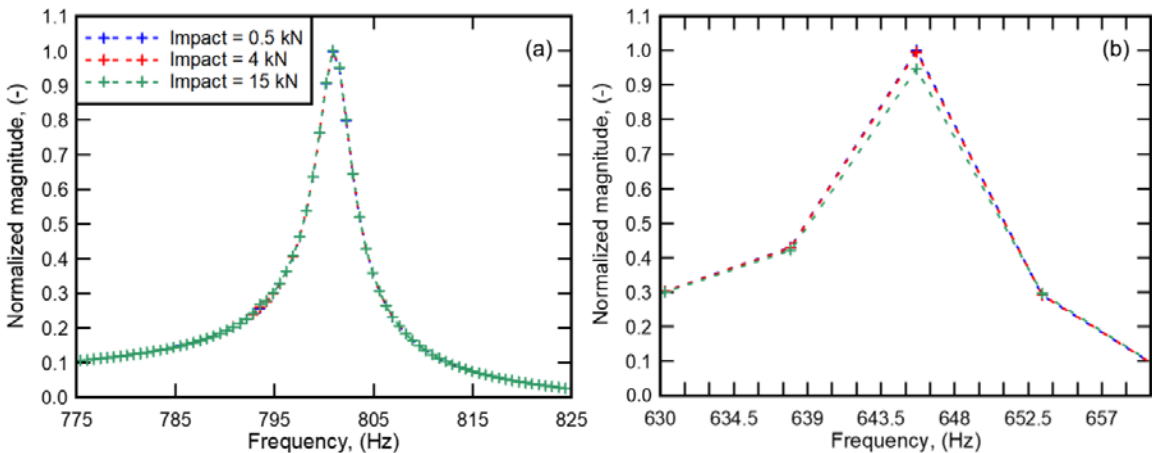
### 3.3.2 Results and Discussion

Fig. 22 shows the FRFs of the simulated beams with and without delamination, i.e., Model 2 and Model 1, respectively, due to an impact force with an amplitude of 4 kN (0.9 kip). While it is expected that the natural frequencies of the beam change because of the delamination, the interpretation of the results is not straight forward. As can be seen in Fig. 22, the FRFs look very different for the two models. Not only is there no consistent shift between individual peaks, they also do not have corresponding matches, and exhibit notable differences in their half-power bandwidths. The latter implies higher inherent damping in the system. In conclusion, a delamination has a significant effect on the measured vibration response. However, because the proposed method is self-referencing, this is not relevant.



**Fig. 22.** Two sample FRFs for deck models with and without delamination; amplitude of impact force = 4 kN (0.9 kip).

As can be observed in Fig. 23 (a), the FRF response of the beam model without delamination for a select peak does not change due to an increasing impact force with amplitudes ranging from 0.5 to 15 kN (0.11 to 3.37 kip). On the other hand, increasing the value of the impact force does cause notable changes in the FRFs of the beam model with a delamination. This effect manifests as a change in the magnitude of the selected FRF peaks where the magnitude decreases with increasing impact force, as can be observed in Fig. 23 (b).



**Fig. 23.** Three sample FRF peaks (first peak) for impact forces with amplitudes, 0.5, 4 and 15 kN (0.112, 0.9, and 3.37 kip): (a) Model 1 (without delamination, reference) and (b) Model 2 (with delamination).

Fig. 24 shows a comparison of the FRF peak ratios, which corresponds to the FRF peak value normalized with the FRF peak value for the smallest impact force of 0.5 kN (0.112 kip), for both beam models. For Model 1 (reference case), it can be observed that there is a minute increase in the peak response, which can likely be attributed to the nonlinear

material response of concrete (see Section 3.4.3 for further discussion). Model 2 (delamination case), however, shows a clear decrease in the peak response after the force exceeds approximately 3 kN (0.674 kip). This behavior can be associated with contact interaction of the lower and upper boundaries of the simulated delamination when the vibration amplitude of these boundaries exceeds the width of the delamination. The numerical simulations show that changes of the FRF are sensitive to the presence of a delamination. It can be speculated that other types of damage and degradation have a similar but smaller effect.

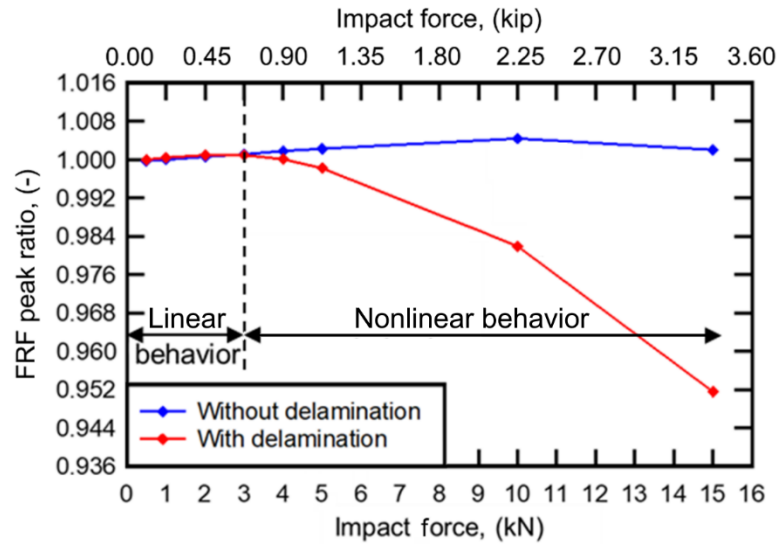
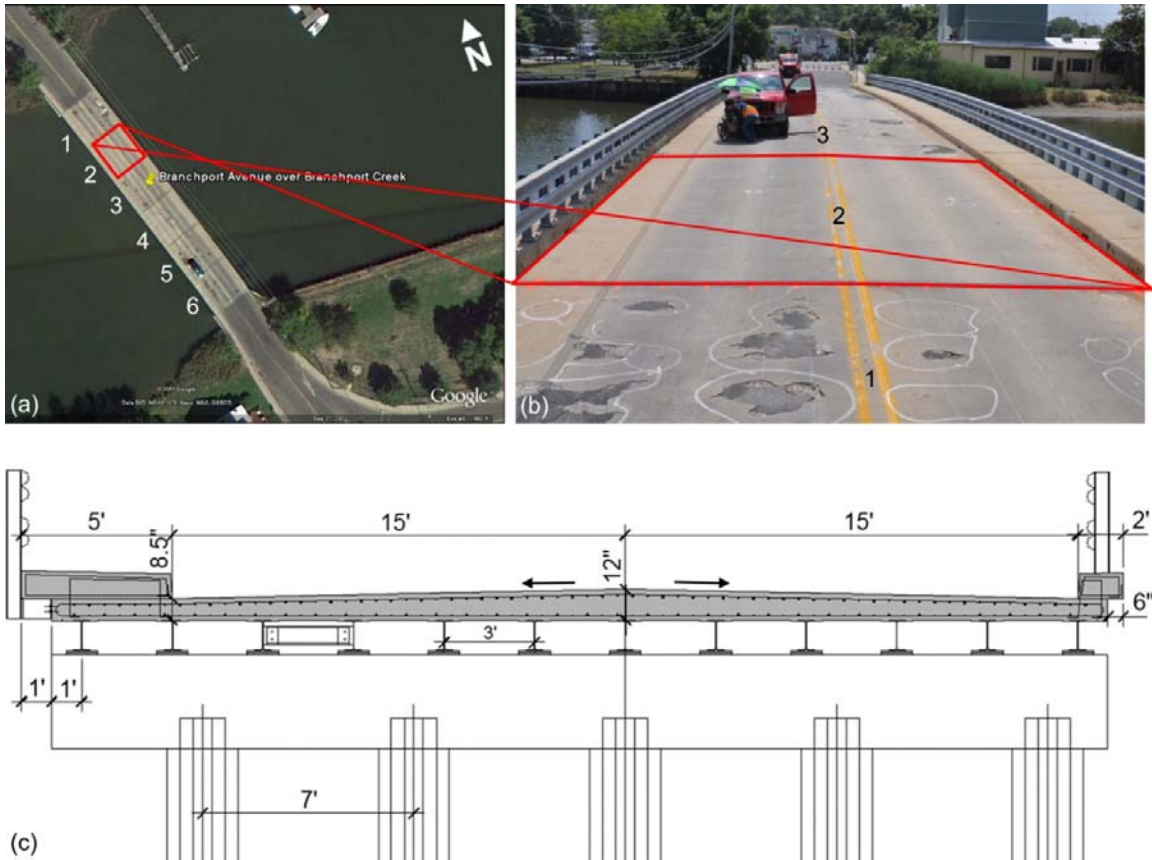


Fig. 24. FRF peak ratio vs. peak impact force value for the two FE models.

### 3.4 Experimental Study

#### 3.4.1 Description of Structure Used for Evaluation

A steel-concrete composite bridge located in Branchport, NJ, USA was selected to evaluate the proposed method's ability to detect damaged areas in an in-service reinforced concrete bridge deck. The bridge, presented in Fig. 25, has a total length of 65.8 m (216 ft) and is 11.3 m (37 ft) wide. The superstructure consists of six 11.0 m (36 ft) long two-span sections with steel girders carrying a 216 to 305 mm (8.5 to 12 in) thick reinforced concrete deck, as shown in Fig. 25 (c). Due to the harsh environment combined with exposure to chlorides from seawater and deicers, the bridge exhibited severe distress when it was visually inspected in July 2011. Five of the six deck sections were found to have severe surface damage, showing visible signs of spalling, potholes, and in some locations the steel rebars were exposed. The deck selected for this study (#2, highlighted in Figs. 25 (a) and b) showed no visual distress and hammer sounding revealed only two small areas potentially having delaminations [see Fig. 26 (a)].



**Fig. 25.** Branchport Avenue Bridge in Long Branch, NJ: (a) Google map image showing plan view and selected deck (#2) used as part of this study, (b) photo of Deck #2 from a driver's perspective, and (c) bridge cross-section with dimensions in (in = ")

Unit conversion: 1 in = 25.4 mm, 1 ft = 0.305 m.

Since the responsible County had planned to rehabilitate the entire bridge deck, this represented an opportunity to evaluate a variety of NDT methods by comparing their results with the removed concrete. Findings are reported in Clem (2013) and Celaya et al. (2014). The NDT surveys, including the IR testing discussed in this research, were completed in July 2011; hydro-blasting to remove surface as well as damaged concrete was performed in March 2013. Before new concrete was placed in July 2013, the depth of the removed concrete was measured on a 610 x 610 mm (2 x 2 ft) grid. Depth measurements were established using traditional surveying equipment and made available by Cherry, Weber & Associates.

### 3.4.2 Test Setup and Procedure

A typical impulse response (IR) test setup was used, as illustrated in Figs. 3 and 18. The hammer (PCB, Model 086D20) weighs 0.67 kg (1.5 lb) and has a 51 mm (2 in) diameter

hard-plastic hammer tip [ $\pm 22.2$  kN-peak (5000 lb-peak)]. It is equipped with a piezoelectric load cell connected to a signal amplifier/conditioner to measure the generated impact force. The vibration response was measured using a capacitive MEMS accelerometer (Silicon Designs-Model-2260-010) that has a flat frequency response within 3 dB over the range of 0 to 1 kHz. Both input (force) and output (acceleration) signals were recorded using a high-speed transient recorder (Elsys, Model TraNET 204s) with a sampling frequency of 500 kHz.

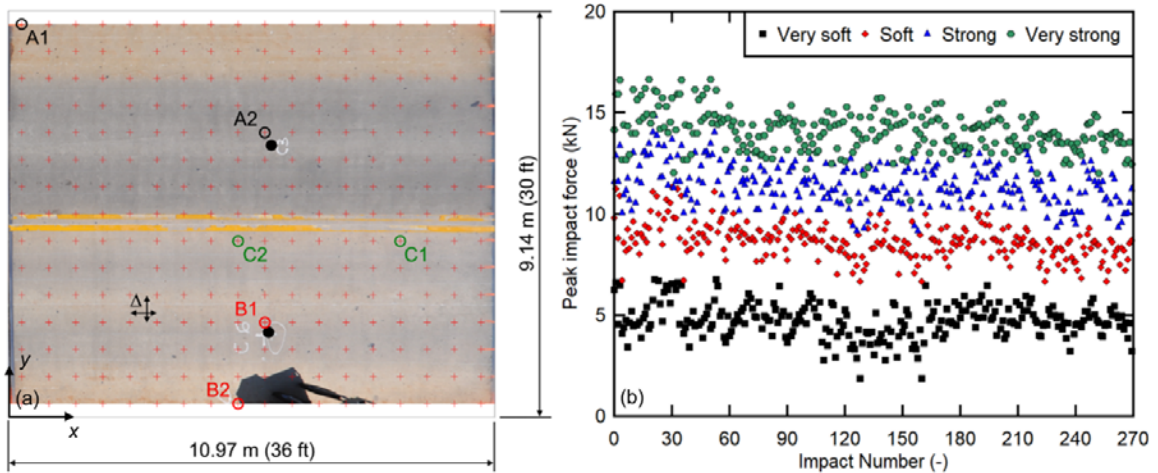


**Fig. 26.** (a) Plan view photo of Deck #2 with test grid (red '+'),  $\Delta = 0.61$  m (2 ft), locations of sample test points A1, A2, B1, B2, C1, and C2, and extracted concrete cores (full black circles). (b) Peak impact forces for all 270 test points. Unit conversion: 20 kN = 4.5 kip.

The two-lane traffic portion of Deck #2, measuring 9.14 x 11.0 m (30 x 36 ft), was divided into a 610 x 610 mm (2 x 2 ft) test grid, resulting in 270 individual test points, as shown in Fig. 26 (a). Two locations were selected for concrete coring and are highlighted by solid black circles. Four hammer impacts were applied at each test point manually, i.e., by a human operator, with increasing amplitude, referred to as “very soft”, “soft”, “strong”, and “very strong”, as illustrated in Fig. 26 (b). Sample results from the proposed test method are shown as colored circles and marked A1, A2, B1, B2, C1, C2 [see Fig. 26 (a)] and are discussed in detail in Section 3.5.1.

Fig. 27 shows sample time histories of four impact forces with different levels of amplitude and the corresponding acceleration responses for one select test point.

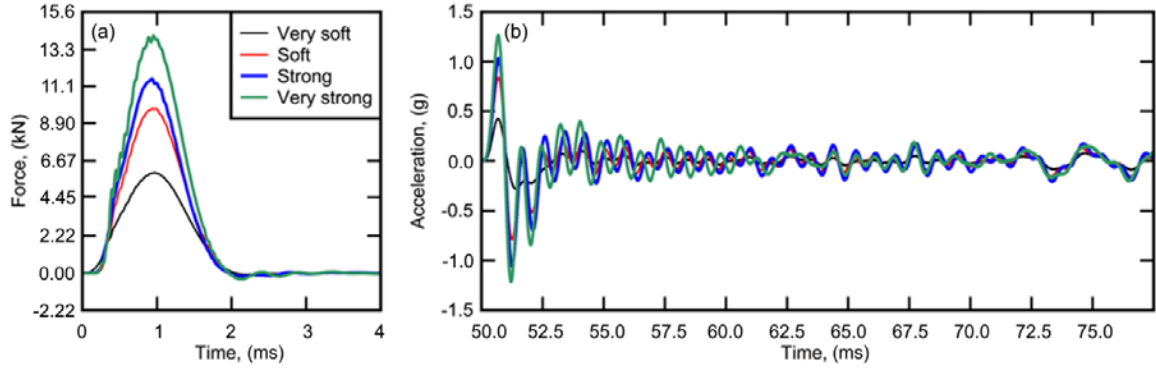


**Fig. 27.** Samples of (a) four impact forces and (b) corresponding acceleration responses for one select test point. Unit conversion: 15.6 kN = 3.5 kip.

### 3.4.3 Sources of Nonlinearity

Structural systems may exhibit nonlinear vibrations due to several factors (Farrar and Worden 2013). For the system investigated in this study, two factors are considered: Material nonlinearity and crack boundary interaction. The former is due to the nonlinear stress-strain relationship of concrete. To ensure that the proposed NVI is not affected by this nonlinearity, the stresses generated from the impact forces were calculated and compared with the theoretical concrete stress-strain relationship proposed by Carreira and Chu (Carreira and Chu 1985).

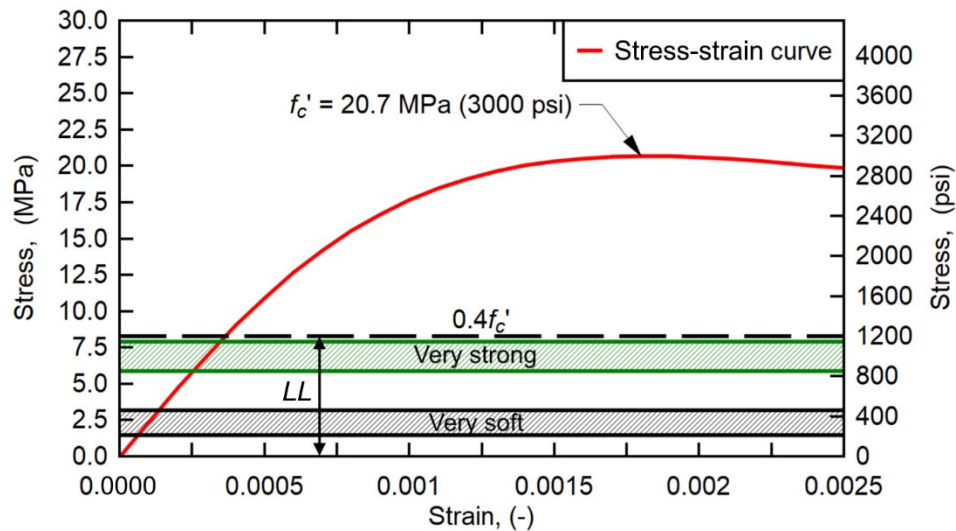


**Fig. 28.** Theoretical Stress-Strain relationship and actual generated stress ranges due to “very soft” (grey area) and “very strong” (green area) impact forces (ranges span mean +/- two standard deviations). The black dashed horizontal line represents the suggested linear limit (LL).

Fig. 28 shows this stress-strain relationship, which assumes a conservative concrete compressive strength,  $f_c' = 20.7$  MPa (3,000 psi). It can be observed that all generated stresses lie within the suggested linear limit ( $LL$ ) of 40% of  $f_c'$  (shown as black dashed line) (fib 2010). The ranges of generated stresses for “very soft” and “very strong” impact forces spanning the means +/- two standard deviations taken from data shown in Fig. 26 (b) are provided for reference. To conclude, effects due to material nonlinearity can be assumed to have a negligible effect on the proposed nonlinearity parameter, NVI.

Cracks resulting from concrete degradation is the second factor leading to nonlinearity, and of interest to this study. Cracks open and close during vibrations, leading to a complex dynamic response when the crack boundaries interact, which has been referred to as crack breathing (Giannini et al. 2014). Although the cracks are initially small and distributed, they may grow and coalesce to eventually form a localized macro crack such as a shallow delamination in a concrete bridge deck. As demonstrated in Section 3.3, the proposed NVI should theoretically be able to detect this type of damage. While a delamination is distinctly different from distributed micro cracks, the crack breathing model still applies; in fact, it can be hypothesized that it is much more pronounced for this case.

To conclude, since material nonlinearity is deemed negligible, only cracking-related degradation should affect the NVI. Furthermore, it is assumed that the stress-strain relationship does not have a notable effect on detectability of concrete degradation such as a delamination.

### **3.5 Results and Discussion**

#### **3.5.1 Verification of Results from Individual Test Points**

As has been reported, the crack boundary interaction of a delamination can cause nonlinear vibrations due to the effects of the crack breathing phenomenon (Giannini et al. 2014). In this section, results from six test points on Deck #2 were selected and are discussed in detail to evaluate the proposed test method. The six test points were divided into three groups (A, B, and C) according to the observed results from the proposed method, available cores, and visual inspection (see Fig. 26 (a) for test point locations). Each group consists of two test points (see Table 1). Note that “very soft” serves as the reference case for the three other impact forces, namely “soft”, “strong”, and “very strong”. The level of nonlinearity of the tested locations, which is represented by the NVI, was computed over a frequency range of  $f_1 = 225$  to  $f_2 = 500$  Hz. The lower limit,  $f_1$  of this subjective range was chosen to exclude low-frequency noise caused by traffic, wind, etc. The upper limit,  $f_2$  was selected to minimize the effect of nonlinearity introduced by the used accelerometer. In a previous

study the authors used the same instrumentation and found this type of nonlinear vibration response to start at approximately 600 Hz (Hafiz and Schumacher 2019). Therefore, the upper limit was conservatively set at 500 Hz.

**Table 1.** Six selected test point coordinates and their NVI; “very soft” = reference case.

Group	Location [see Fig. 26 (a)]	x [m (ft)]	y [m (ft)]	NVI (-)		
				Soft	Strong	Very strong
A	A1	0.305 (1.00)	8.84 (29.0)	0.99	0.98	0.98
	A2	5.79 (19.0)	6.40 (21.0)	0.98	0.98	0.97
B	B1	5.79 (19.0)	2.13 (7.00)	0.63	0.49	0.44
	B2	5.18 (17.0)	0.305 (1.00)	0.96	0.91	0.98
C	C1	8.84 (29.0)	3.96 (13.0)	0.38	0.25	0.05
	C2	5.18 (17.0)	3.96 (13.0)	0.89	0.88	0.86

Group A represents two test points that were not found to have any form of degradation by visual inspection. Fig. 19 shows the FRF for test point A1, as well as the peak impact forces. Recall from the discussion in Section 3.3, although the impact force was more than doubled, this only had a very minor effect on the FRF, which implies the system is linear. Fig. 20 shows the  $R^2$ -frequency relationship for test point A1, which is close to 1, indicating near linear behavior. Similarly, the  $R^2$ -frequency relationship of test point A2 is also not significantly affected by the increase of the impact force, as can be observed in Fig. 29 (a). Since any structure will demonstrate a certain level of nonlinearity, 3% can be interpreted as the uncertainty in the NVI value for non-degraded concrete in this study. The concrete core taken near test point A2 is further proof that this location is in healthy condition, i.e., not showing any delamination, as can be seen in Fig. 30 (a). In conclusion, areas on the bridge deck that do not show signs of nonlinear vibration behavior can be considered healthy, i.e., free of degradation or delaminations, which supports the basic idea behind the proposed method.

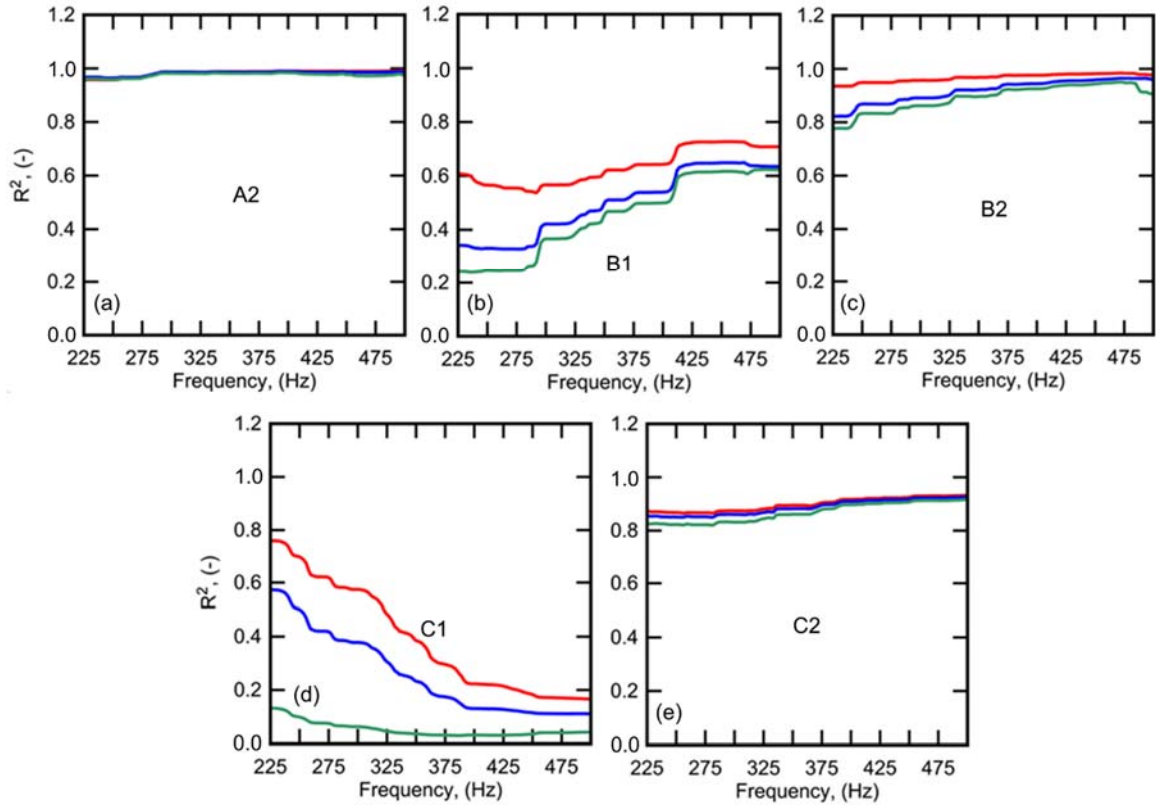


**Fig. 29.**  $R^2$ - frequency relationships for test point A2 (a), B1 (b), B2 (c), C1 (d), and C2 (e). Locations of these test points are shown in Fig. 26 (a). Photos of extracted cores corresponding to (a) and (b) are shown in Fig. 30. Note that the  $R^2$ - frequency relationships for test point A1 is shown in Fig. 20.

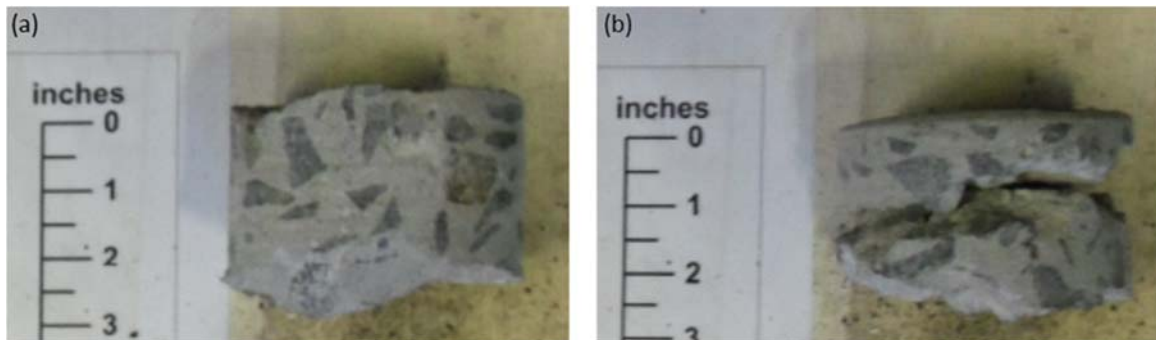


**Fig. 30.** Photos of extracted concrete cores: (a) Core 1 (near A2) and (b) Core 2 (near B1).

Group B represents two test points that were marked having delaminations by means of chain drag. The  $R^2$ - frequency relationships for the Group B test points are presented in Figs. 29 (b) and (c). It can be observed that the responses are significantly affected with increasing impact force, leading to low  $R^2$  functions. Additionally, along with an increase in the amplitude of the impact force, the change in the  $R^2$ - frequency relationship increases,

resulting in a decrease in the NVI value, as shown in Table 1. This response is distinctly different from the one found in Group A. These results also match the core taken near test point B1, which shows a horizontal crack at a depth of approximately 25 mm (1 in) [see Fig. 30 (b)]. In conclusion, the Group B results further confirm that the proposed method can detect delaminations. The NVI values for test point B2 are not as low as for B1, which is where visual inspection found a small, delaminated area [see Fig. 26 (a)].

Group C represents two test locations that exhibited nonlinear vibration behavior, but where the visual inspection did not find any degradation or delaminations. The two associated test points exhibited strong nonlinear vibration behavior, as shown in their FRFs [see Figs. 29 (d) and (e)]. Unfortunately, no cores were available for the Group C test locations. However, the NVI values could be compared with the depth of the removed concrete after hydro-blasting was performed, which is discussed in more detail in Section 3.5.2. The depth of removed concrete for these locations was approximately 40 mm (1.6 in) for C1 and C2, which can be considered relatively high. Assuming that hydro-jetting removes more depth when the concrete is degraded, i.e., having distributed micro cracks, the hypothesis that the NVI method can detect degradation is also supported.

Since only two cores were available for the entire deck, a comparison between the NVI results and the depth of removed concrete was the only way to evaluate the proposed method for all 270 test points, which is discussed in the subsequent section.

### **3.5.2 Comparison of Results with Removed Concrete**

Fig. 31 shows contour plots of (a) NVI values and (b) depth of removed concrete by hydro-blasting across the entire Deck #2. NVI values were computed between the “very soft” (= reference) and “very strong” impact forces. Both NVI results and depth of removed concrete agree in that there is a large degraded or delaminated area along the centerline of the deck as highlighted by the black dashed box. Additionally, both figures show that the area highlighted by the gray dashed boxes are in good condition. On the other hand, the NVI method missed a literal hole in the deck found after hydro-blasting had been completed, as highlighted by the red dashed box. This, however, makes sense, since a hole is simply the case of material missing in some area, which is not the same as an area of degraded concrete. Also, several low NVI values, e.g., around  $x = 5.49$  to  $6.71$  m (18 to 22 ft) and  $y = 0.91$  to  $2.13$  m (3 to 7 ft), which would point to degradation or delamination, are visible that could not be associated with a high depth of removed concrete.

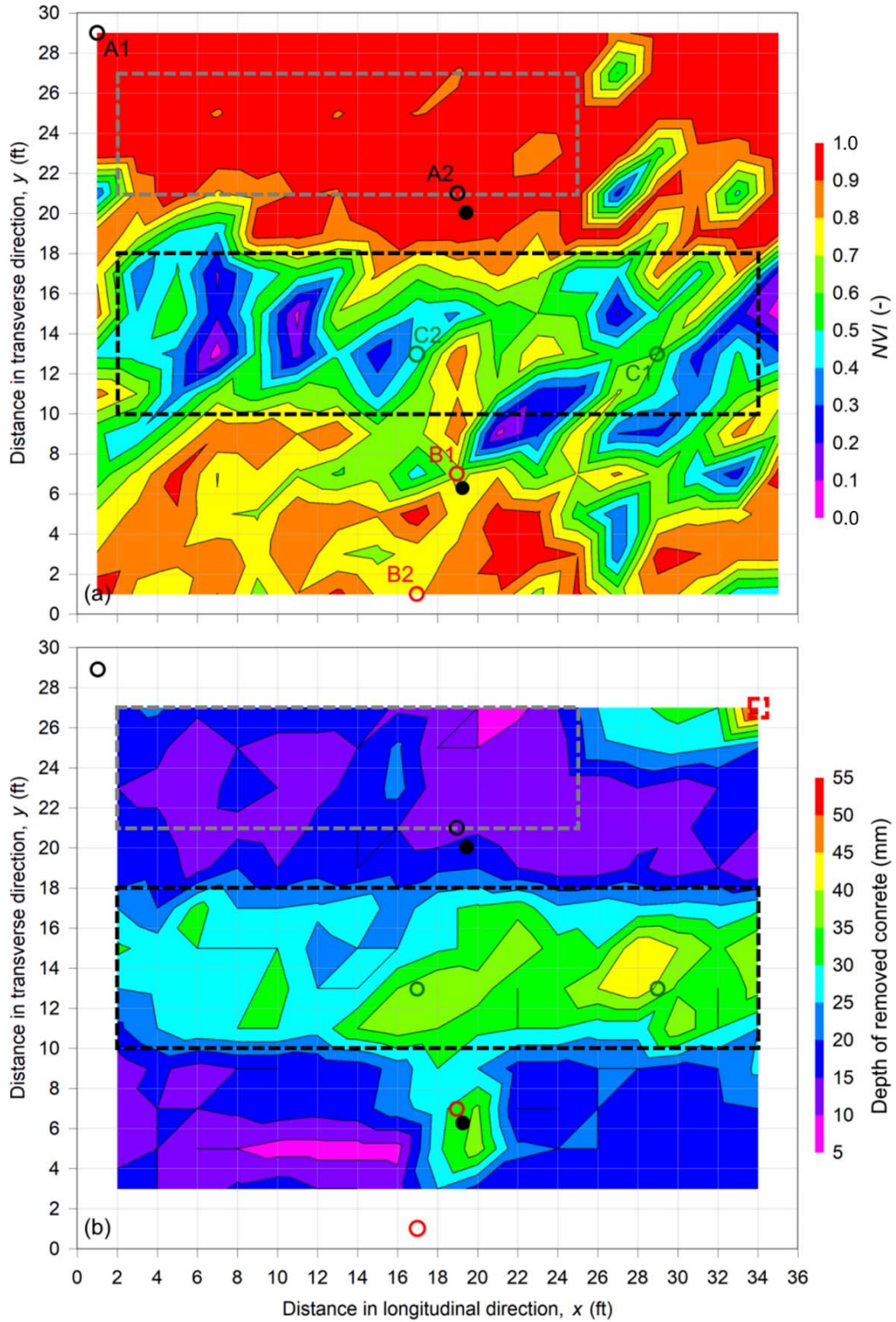


**Fig. 31.** Contour plots for (a) NVI values and (b) depth of removed concrete for Deck #2. Circles depict select test points discussed in more detail in Section 3.5.1. Unit conversion: 1 ft = 0.305 m.

Note that the NVI value for test point B1 was consistent with the nearby concrete core that was found to have a delamination, as is discussed in Section 3.5.1. The discrepancy away from this test point highlights the need for additional research to better understand other factors not yet considered.

Fig. 32 shows a correlation plot between NVI values and depth of removed concrete. The data behind this plot were generated by interpolating the two datasets shown Fig. 31 over a range  $x = 0.610$  to  $10.4$  m (2 to 34 ft) and  $y = 0.914$  to  $8.23$  m (3 to 27 ft) using the generate mesh function with planar interpolation available in DPlot (Hyde 2014). Linear least-squares regression was performed on these data to determine the mean prediction curve (red dash-dotted line) and 95% prediction limits (blue dotted lines). While a linear relationship with statistical significance at the 95% confidence level exists, the correlation coefficient,  $R = -0.532$  is low and considerable scatter is present. As such, this relationship should only be interpreted as an indication of an overall trend. Orange and blue dots correspond to data points from within the grey and black dashed boxes, respectively, shown in Fig. 31, and the red dot corresponds to the location of the hole discussed earlier [at  $x = 10.4$  m (34 ft),  $y = 8.23$  m (27 ft)].

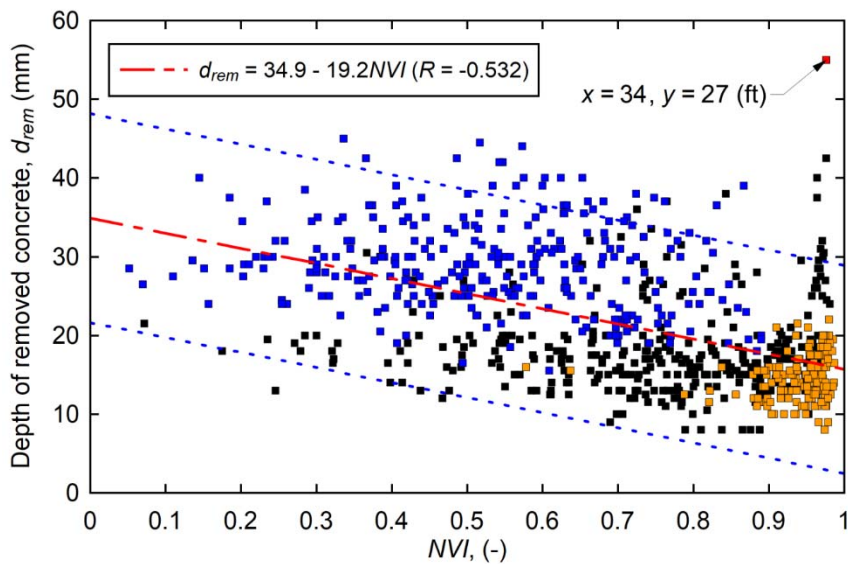


**Fig. 32.** NVI - Depth of removed concrete vs. NVI correlation plot. Orange and blue dots correspond to data points from within the grey and black dashed boxes, respectively, shown in Fig. 31. The red dash-dotted line and blue dotted lines represent the mean prediction curve and 95% prediction limits, respectively. Unit conversion: 1 ft = 0.305 m.

While it can be concluded that the NVI cannot be directly used to predict the amount of removed concrete during hydro-blasting, Fig. 32 nonetheless indicates that the proposed

method is not only capable of detecting the onset of delaminations but may also be sensitive to distributed damage. Note that a data analysis following conventional IR parameters (ASTM 2016) did not reveal any of these issues (Clem 2013).

### **3.6 Summary and Conclusions**

The presented results demonstrate the potential for the proposed nonlinear vibration index (NVI) method to detect degradation and delamination in reinforced concrete bridge decks. The NVI method is based on the concept of deviation from linearity, which is determined by computing the frequency response functions (FRFs) for a set of increasing impact forces applied to a specific test point and comparing them via correlation coefficients. The hypothesis is that if the FRFs remain constant and change, this can be associated with healthy and degraded or damaged areas, respectively. A numerical study using a finite element (FE) model demonstrated that nonlinear behavior was indeed exhibited for a deck with a delamination when subject to increasing impact forces. The proposed method was then evaluated using data from an in-service bridge deck. The equipment is the same as is used for impulse response (IR) tests on concrete plates. The results of the field study support the proposed hypothesis. A comparison between NVI results and visual inspection results, extracted concrete cores for six test locations, as well as depth of removed concrete from hydro-blasting was performed. The final observations and conclusions are as follows:

- NVI results were able to distinguish healthy areas in the bridge deck with ones that had degradation or delaminations. Additionally, NVI results were in excellent agreement with visual inspection and core test results.
- A strong match was found between the results of the NVI method and visual inspection and cores for detecting areas that could potentially have degradation or delamination.
- A qualitative comparison between NVI values and depth of removed concrete showed acceptable agreement in terms of areas of degradation or delaminations.
- An overall trend was found between NVI values and depth of removed concrete. While notable scatter exists, a linear regression revealed a trend consistent with the proposed hypothesis. Note that the mean prediction equation found through linear least-squares regression should not be used to predict depth of removed concrete.

It should be noted that the proposed method, at this point, cannot distinguish between type of damage. Additional research is required before predictions with respect to type of damage and depth of removed concrete can be made reliably. Future research includes additional modeling and laboratory research to establish firm relationships as well as define the limitations of the method. For example, additional scenarios should be studied where

crack depth, crack extent, applied force, etc. are varied, to ensure the method works under many possible configurations in the field.

### **3.7 Acknowledgements**

The Higher Committee for Education Development (HCED) in Iraq supported the first author of Hafiz et al. (2022) during his PhD studies. Test equipment was made available by the Department of Civil and Environmental Engineering at the University of Delaware. The data analyzed in this research were collected as part of a research project sponsored by the Delaware Department of Transportation (DelDOT). Further thanks go to Lassaad Mhamdi, Daniel J. Clem, Tayler C. Wennick, and Kaitlyn N. Gisonda for assisting with data collection. Access to the bridge as well as traffic management during testing was provided by Kaz Tabrizi and Manuel Celaya from Advanced Infrastructure Designs and Greg Bitsko from Cherry, Weber & Associates, and are greatly appreciated.

## 4 SUMMARY AND CONCLUSIONS

In this research, two easy-to-deploy non-destructive test (NDT) methods were evaluated for detecting deterioration - in particular, delaminations - in reinforced concrete bridge decks, namely ground penetrating radar (GPR) and impulse response (IR) testing.

To evaluate the detection capabilities of GPR, three laboratory specimens were constructed, and scanned using a 1.6 GHz frequency hand-held instrument. In a laboratory setting, and using the proposed cross-correlation methodology, it was possible to distinguish reflections from air, water, or steel through 154 mm (6.06 in) of unreinforced concrete by their polarity and amplitude and detect an air gap of 3.2 mm (0.126 in) between two 154 mm (6.06 in) thick unreinforced concrete blocks. Rebar depths could be detected reliably over a range of approximately 25 mm to 200 mm (1 to 8 in). The thickness of Specimens 1a and b could be estimated accurately because there was only one layer of top reinforcing bars spaced at approximately 200 mm (8 in). The embedded artificial shallow delamination in Specimen 2 was correctly identified. The depth of reflectors could be located with an overall accuracy of 16 mm (0.63 in) based on 95% prediction limits. An overall trend between reflected pulse amplitude and rebar depth could be observed. Finally, GPR scans were performed on an in-service concrete bridge deck experiencing significant deterioration. While helpful in some cases, delaminations were not visible in all locations where hammer sounding had predicted them.

IR testing was applied to an in-service bridge experiencing significant deck deterioration in form of delaminations. Deck (#2) was selected because visual inspection and hammer sounding had not found notable areas of delamination. Moreover, the results reported in Clem (2015), which are based on conventional IR parameters, did not reveal any areas of delamination. Because some deterioration was still expected to be present in this deck, which was based on the condition of the other decks, this was an ideal test scenario for a new analysis methodology. This new analysis method produces a so-called nonlinear vibration index (NVI) that is based on nonlinear vibration characteristics. The NVI method is based on the concept of deviation from linearity, which is determined by computing the frequency response functions (FRFs) for a set of increasing impact forces applied to a specific test point and comparing them via correlation coefficients. The concept is that if the FRFs remain constant and change, this can be associated with healthy and degraded or damaged areas in the deck, respectively. A finite element (FE) study was first performed to proof the concept. The results of the field study support the proposed hypothesis. A comparison between NVI results and visual inspection results, extracted concrete cores for

six test locations, as well as depth of removed concrete from hydro-blasting was performed. NVI values helped to distinguish healthy areas in the bridge deck with ones that had degradation or delaminations. A strong match was also found between the results of the NVI method and visual inspection and cores for detecting areas that could potentially have degradation or delamination. Finally, an overall trend was found between NVI values and depth of removed concrete.

Future research should look at improved imaging methods for GPR and the possibility of fusing GPR images with ultrasonic echo array (UEA) images, as it is, e.g., proposed in Mehdinia et al. (2022). For IR testing, additional research should be performed to determine the NVI method's ability to distinguish between damage types. For this, additional modeling, and laboratory work to establish firm relationships as well as define the limitations of the method, are required.

## 5 REFERENCES

- Abdelkhalek, S. and T. Zayed (2020). "Comprehensive Inspection System for Concrete Bridge Deck Application: Current Situation and Future Needs." *ASCE Journal of Constructed Facilities* 34(5): 03120001.
- ACI (2013). ACI 228.2R-13: Nondestructive Test Methods for Evaluation of Concrete in Structures. Farmington Hills, MI, American Concrete Institute.
- Alani, A. M., M. Aboutalebi, et al. (2013). "Applications of ground penetrating radar (GPR) in bridge deck monitoring and assessment." *Journal of Applied Geophysics* 97: 45-54.
- Arndt, R. W., T. Schumacher, D. Algernon and S.-H. Kee (2011). "Strategies for maintenance of highway bridges in the U.S. - with the support of non-destructive testing and structural health monitoring." *Bautechnik* 88(11): 793-804. DOI: <https://doi.org/10.1002/bate.201101513>.
- ASTM (2016). C1740: Standard Practice for Evaluating the Condition of Concrete Plates Using the Impulse-Response Method. West Conshohocken, PA, ASTM International.
- ASTM (2008). D6087-08: Standard Test Method for Evaluating Asphalt-Covered Concrete Bridge Decks Using Ground Penetrating Radar. West Conshohocken, PA, ASTM International.
- Barnes, C. L. and J.-F. Trottier (2000). "Ground-Penetrating Radar for Network-Level Concrete Deck Repair Management." *ASCE Journal of Transportation Engineering* 126(3): 257-262.
- Beben, D., A. Mordak, et al. (2012). "Identification of viaduct beam parameters using the Ground Penetrating Radar (GPR) technique." *NDT & E International* 49(July): 18-26.
- Benedetto, A. (2013). "A three dimensional approach for tracking cracks in bridges using GPR." *Journal of Applied Geophysics* 97: 37-44.
- Bien, J., J. Krzyzanowski, W. Poprawski, W. Skoczynski and J. Szymkowski (2002). Experimental study of bridge structure dynamic characteristics using periodic excitation. International Conference on Noise and Vibration Engineering. Leuven, Belgium. II: 555-562.
- Binda, L., C. Colla, et al. (1994). "Identification of moisture capillarity in masonry using digital impulse radar." *Construction and Building Materials* 8(2): 101-107.
- Bungey, J. H. (2004). "Sub-surface radar testing of concrete: a review." *Construction and Building Materials* 18(1): 1-8.
- Carreira, D. J. and K.-H. Chu (1985). "Stress-Strain Relationship for Plain Concrete in Compression." *ACI Journal Proceedings* 82(6): 797-804.
- Cassidy, N. J., R. Eddies, et al. (2011). "Void detection beneath reinforced concrete sections: The practical application of ground-penetrating radar and ultrasonic techniques." *Journal of Applied Geophysics* 74(4): 263-276.
- Celaya, M., T. Schumacher, K. Tabrizi, G. Bitsko and P. Shokouhi (2014). Field Verification of Non-destructive Testing Technologies for Condition Assessment of Concrete Bridge Decks: A Case Study. NDE/NDT for Structural Materials Technology for Highway & Bridges. Washington, D.C., ASNT.
- Centurion, S. (2020). STATGRAPHICS. The Plains, VA, STATGRAPHICS Technologies, Inc.

- Chang, C. W., C. H. Lin, et al. (2009). "Measurement radius of reinforcing steel bar in concrete using digital image GPR." *Construction and Building Materials* 23(2): 1057-1063.
- Clem, D. J., Schumacher, T., and Deshon, J. P. (2015). A Consistent Approach for Processing and Interpretation of Data from Concrete Bridge Members Collected with a Hand-Held GPR Device. *Construction and Building Materials*. Vol. 86, pp. 140-148. DOI: <https://doi.org/10.1016/j.conbuildmat.2015.03.105>.
- Clem, D. J., J. S. Popovics, T. Schumacher, T. Oh, S. Ham and D. Wu (2013). Understanding the impulse response method applied to concrete bridge decks. Review of Progress in Quantitative Nondestructive Evaluation. Denver, CO, AIP Conference Proceedings. 1511: 1333-1340. DOI: <https://doi.org/10.1063/1.4789197>.
- Clem, D. J. (2013). Evaluation of impulse response & ground-penetrating radar as a means of non-destructive testing of concrete bridge decks. M.S. Thesis. Newark, DE, University of Delaware. URL: <https://udspace.udel.edu/handle/19716/12952>.
- Davis, A. G. (2003). "The nondestructive impulse response test in North America: 1985-2001." *NDT & E International* 36(4): 185-193.
- Davis, A. G. and C. Germann Petersen (2003). Nondestructive Evaluation of Prestressed Concrete Bridges using Impulse Response. Non-Destructive Testing in Civil Engineering 2003. Berlin, Germany, NDT.net.
- Davis, A. G. and S. A. Robertson (1975). "Economic Pile Testing." *Ground Engineering* 8(3): 40-43.
- Doebbling, S. W., C. R. Farrar and M. B. Prime (1998). "A Summary Review of Vibration-Based Damage Identification Methods." *The Shock and Vibration Digest*.
- Dos Santos, V. R. N., W. Al-Nuaimy, et al. (2014). "Spectral analysis of ground penetrating radar signals in concrete, metallic and plastic targets." *Journal of Applied Geophysics* 100: 32-43.
- Ewins, D. J. (1995). *Modal Testing: Theory and Practice*. New York, John Wiley & Sons Ltd.
- Farrar, C. R. and K. Worden (2013). *Structural Health Monitoring: a Machine Learning Perspective*. West Sussex, UK, John Wiley & Sons, Ltd.
- fib (2010). *Model Code for Concrete Structures*.
- Garrett, S. (2019). "Nondestructive Assessment of Bridge Decks." *Materials Evaluation* 77(4).
- Giannini, O., P. Casini and F. Vestroni (2014). "Nonlinear Harmonic Identification of Cracks in Structures." *Dynamics of Civil Structures* 4: 207-217.
- Gucunski, N., A. Imani, F. Romero, S. Nazarian, Y. Deren, H. Wiggenhauser, P. Shokouhi, A. Taffe and D. Kutrubes (2013). *Nondestructive Testing to Identify Concrete Bridge Deck Deterioration*. Washington, D.C., Transportation Research Board.
- Gucunski, N., F. Romero, et al. (2011). *Comprehensive Bridge Deck Deterioration Mapping of Nine Bridges by Nondestructive Evaluation Technologies*. Final Report SPR-NDEB(90)--8H-00 Iowa State Department of Transportation.
- Gucunski, N., C. Rascoe, et al. (2009). *Complementary Condition Assessment of Bridge Decks by High-Frequency Ground-Penetrating Radar and Impact Echo*. Transportation Research Board 88th Annual Meeting. Washington, D.C.
- Dassault Systemes (2012). *ABAQUS 6.12*.

- Hafiz, A., Schumacher, T., and Raad, A. (2022). A Self-Referencing Non-Destructive Test Method to Detect Damage in Reinforced Concrete Bridge Decks Using Nonlinear Vibration Response Characteristics. *Construction and Building Materials*. Vol. 318, Article 125924. DOI: <https://doi.org/10.1016/j.conbuildmat.2021.125924>.
- Hafiz, A. and T. Schumacher (2019). "Effects of Elastic Supports and Flexural Cracking on Low and High Order Modal Properties of a Reinforced Concrete Girder." *Engineering Structures* 178: 573-585. DOI: <https://doi.org/10.1016/j.engstruct.2018.10.041>.
- Hong, S. X., W. L. Lai, et al. (2012). Monitoring accelerated corrosion in chloride contaminated concrete with ground penetrating radar. 14th International Conference on Ground Penetrating Radar (GPR). Shanghai, China: 561-566.
- Hugenschmidt, J. and R. Loser (2007). "Detection of chlorides and moisture in concrete structures with ground penetrating radar." *Materials and Structures* 41(4): 785-792.
- Hyde, D. (2014). DPlot. Vicksburg, MS, HydeSoft Computing LLC.
- Idriss, M., A. El Mahi and R. El Guerjouma (2015). "Characterization of Sandwich Beams with Debonding by Linear and Nonlinear Vibration Method." *Composite Structures* 120: 200-207.
- Kee, S.-H. and N. Gucunski (2016). "Interpretation of Flexural Vibration Modes from Impact-Echo Testing." *ASCE Journal of Infrastructure Systems* 22(3): 04016009.
- Kee, S.-H., T. Oh, J. S. Popovics and R. W. Arndt (2012). "Nondestructive Bridge Deck Testing with Air-Coupled Impact-Echo and Infrared Thermography." *ASCE Journal of Bridge Engineering* 17(6): 928-939.
- Kerschen, G., K. Worden, A. F. Vakakis and J.-C. Golinval (2006). "Past, Present and Future of Nonlinear System Identification in Structural Dynamics." *Mechanical Systems and Signal Processing* 20(3): 505-592.
- Lai, W. L., T. Kind, et al. (2011). "Frequency-dependent dispersion of high-frequency ground penetrating radar wave in concrete." *NDT & E International* 44(3): 267-273.
- Lin, R. (1990). Identification of the Dynamic Characteristics of Nonlinear Structures. PhD, University of London.
- Lin, S., H. Azari, D. Meng and S. Shams (2021). Nondestructive Evaluation of Concrete Bridge Decks with Overlays. Washington, D.C., FHWA Turner-Fairbank Highway Research Center.
- Liu, C.-J., M. D. Todd, Z.-L. Zheng and Y.-Y. Wu (2017). "A Nondestructive Method for the Pretension Detection in Membrane Structures Based on Nonlinear Vibration Response to Impact." *Structural Health Monitoring* 17(1): 67-79.
- Louis, A., A. Van Der Wielen, et al. (2012). GPR detection of saturated areas into concrete in the presence of a water gradient. 14th International Conference on Ground Penetrating Radar (GPR). Shanghai, China: 473-478.
- Maser, K. (1996). "Condition Assessment of Transportation Infrastructure Using Ground-Penetrating Radar." *Journal of Infrastructure Systems* 2(2): 94-101.
- Mathworks (2020). MATLAB. Natick, MA, Mathworks.
- Mehdinia, S., Schumacher, T., Wan, E., and Song, X. (2022). A Pipeline for Enhanced Multimodal 2D Imaging of Concrete Structures. *Materials and Structures* 54(6): 228. DOI: <https://doi.org/10.1617/s11527-021-01803-w>.

- Muniappan, N., A. V. Hebsur, et al. (2012). Radius estimation of buried cylindrical objects using GPR: A case study. 14th International Conference on Ground Penetrating Radar (GPR). Shanghai, China: 789-794.
- NCHRP (2004). Concrete Bridge Deck Performance - A Synthesis of Highway Practice. NCHRP Synthesis 333. Washington, D.C., Transportation Research Board.
- Noel, J. P. and G. Kerschen (2017). "Nonlinear System Identification in Structural Dynamics: 10 More Years of Progress." *Mechanical Systems and Signal Processing* 83: 2-35.
- Romero, F. A., G. E. Roberts, et al. (2000). Evaluation of GPR Bridge Deck Survey Results Used for Delineation of Removal/Maintenance Quantity Boundaries on Asphalt-Overlaid, Reinforced Concrete Deck. *Structural Materials Technology IV*. S. Alampalli. Atlantic City, NJ, Technomic Publishing Company, Inc.
- Sajid, S. and L. Chouinard (2019). "Impulse response test for condition assessment of concrete: a review." *Construction and Building Materials* 211: 317-328.
- Salawu, O. S. and C. Williams (1995). "Bridge Assessment Using Forced-Vibration Testing." *ASCE Journal of Structural Engineering* 121(2): 161-173.
- Samman, M. M. and M. Biswas (1994). "Vibration Testing for Nondestructive Evaluation of Bridges. I: Theory." *ASCE Journal of Structural Engineering* 120(1): 269-289.
- Samman, M. M. and M. Biswas (1994). "Vibration Testing for Nondestructive Evaluation of Bridges. II: Results." *ASCE Journal of Structural Engineering* 120(1): 290-306.
- Sansalone, M. J. and W. B. Streett (1997). *Impact-Echo - Nondestructive Evaluation of Concrete and Masonry*. Ithaca, NY, Bullbrier Press.
- Scherr, J. F. and C. Grosse (2021). "Delamination detection on a concrete bridge deck using impact echo scanning." *Structural Concrete* 22(2): 806-812.
- Scott, M., A. Rezaizadeh, A. Delahaza, C. G. Santos, M. Moore, B. Graybeal and G. Washer (2003). "A Comparison of Nondestructive Evaluation Methods for Bridge Deck Assessment." *NDT & E International* 36(4): 245-255.
- Shah, M. R., S. G. Millard, et al. (2005). "Location of steel reinforcement in concrete using ground penetrating radar and neural networks." *NDT & E International* 38(3): 203-212.
- Shokouhi, P., J. Wolf and H. Wiggenger (2014). "Detection of Delamination in Concrete Bridge Decks by Joint Amplitude and Phase Analysis of Ultrasonic Array Measurements." *ASCE Journal of Bridge Engineering* 19(3): 04013005.
- Soldovieri, F., R. Persico, et al. (2006). "The application of inverse scattering techniques with ground penetrating radar to the problem of rebar location in concrete." *NDT & E International* 39(7): 602-607.
- Stryk, J. (2013). "Possibilities of ground penetrating radar usage within acceptance tests of rigid pavements." *Journal of Applied Geophysics* 97: 11-26.
- Sun, H., J. Zhu and S. Ham (2018). "Automated Acoustic Scanning System for Delamination Detection in Concrete Bridge Decks." *ASCE Journal of Bridge Engineering* 23(6): 04018027.
- Tarussov, A., M. Vandry, et al. (2013). "Condition assessment of concrete structures using a new analysis method: Ground-penetrating radar computer-assisted visual interpretation." *Construction and Building Materials* 38(January): 1246-1254.
- Underwood, S. S., J. J. Meyer and D. E. Adams (2015). "Damage Localization in Composite Structures Using Nonlinear Vibration Response Properties." *Journal of Vibration and Acoustics* 137(3): 031015.

- Valle, S., L. Zanzi, et al. (1999). "Radar tomography for NDT: comparison of techniques." *Journal of Applied Geophysics* 41(2-3): 259-269.
- Viriyametanont, K., S. Laurens, et al. (2008). "Radar survey of concrete elements: Effect of concrete properties on propagation velocity and time zero." *NDT & E International* 41(3): 198-207.
- Xie, X., H. Qin, et al. (2013). "An automatic recognition algorithm for GPR images of RC structure voids " *Journal of Applied Geophysics* 99: 125-134.
- Xie, X., P. Li, et al. (2012). GPR identification of voids inside concrete based on support vector machine (SVM) algorithm. 14th International Conference on Ground Penetrating Radar (GPR). Shanghai, China: 381-386.
- Zhang, G., R. S. Harichandran and P. Ramuhalli (2012). "Automatic Delamination Detection of Concrete Bridge Decks Using Impact Signals." *ASCE Journal of Bridge Engineering* 17(6): 951-954.
- Zhao, X. Y., Z.-Q. Lang, G. Park, C. R. Farrar, M. D. Todd, Z. Mao and K. Worden (2015). "A New Transmissibility Analysis Method for Detection and Location of Damage via Nonlinear Features in MDOF Structural Systems." *IEEE/ASME Transactions on Mechatronics* 20(4): 1933-1947.
- Zhou, H. F., Y. Q. Ni and J. M. Ko (2011). "Eliminating Temperature Effect in Vibration-Based Structural Damage Detection." *ASCE Journal of Engineering Mechanics* 137(12): 785-796.
- Zhou, Z., L. D. Wegner and B. F. Sparling (2007). "Vibration-Based Detection of Small-Scale Damage on a Bridge Deck." *ASCE Journal of Structural Engineering* 133(9): 1257-1267.